



Nonuniversal structure of point defects in face-centered cubic metals

Pui-Wai Ma * and S. L. Dudarev 

UK Atomic Energy Authority, Culham Science Centre, Oxfordshire, OX14 3DB, United Kingdom



(Received 17 October 2020; accepted 21 December 2020; published 11 January 2021)

Using *ab initio* density function theory calculations, we have determined the structure of self-interstitial atom (SIA) defects in the most commonly occurring face-centered cubic (FCC) metals. The most stable SIA defects in Al, Ca, Ni, Cu, Pd, and Ag are the $\langle 100 \rangle$ dumbbells whereas octahedral SIA configurations have the lowest energy in Pt, Rh, and Th. The relative stability of defect configurations in Sr, Ir, Au, and Pb is less well defined, and calculations suggest that an SIA defect has the $\langle 100 \rangle$ dumbbell structure in Sr and Ir, a $\langle 110 \rangle$ crowdion/dumbbell structure in Au, and that it adopts an octahedral configuration in Pb. The occurrence of octahedral and $\langle 110 \rangle$ crowdion/dumbbell SIA configurations implies that defects diffuse one-dimensionally. This is fundamentally different from the three-dimensional translation-rotation migration characterizing the mobility of a $\langle 100 \rangle$ dumbbell. Elastic fields of point defects are defined by their elastic dipole tensors, which we compute for all the defect configurations. The magnetism of a $\langle 100 \rangle$ dumbbell in ferromagnetic nickel appears to have little effect on the structure of the defect. The variation of energy and elastic field of an SIA defect in copper is explored in detail as a function of its structural transformation along the migration pathway.

DOI: [10.1103/PhysRevMaterials.5.013601](https://doi.org/10.1103/PhysRevMaterials.5.013601)

I. INTRODUCTION

Face-centered cubic (FCC) metals are widely used in nuclear engineering and technology. Lead (Pb) is a well known shielding material for x-ray and γ -ray applications. Aluminum (Al) and its alloys have been used as materials for nuclear fuel cladding [1]. Copper (Cu), silver (Ag), and gold (Au) are group 11 elements. They are characterized by high corrosion resistance and high electric conductivity and are extensively used in electronics. Copper alloys, including CuCrZr, are the heat sink materials for fusion tokamak divertor applications where they serve as interfaces between the plasma facing tungsten components and the coolant [2,3].

Crystalline materials do not retain their perfect structural order in an environment where they are exposed to the bombardment by energetic particles. Following an initial impact and subsequent dynamic evolution and relaxation of atomic positions, the initial crystalline order is partially restored, but in most cases, the recovery is incomplete. The remaining imperfection of the lattice structure can be identified and classified as various crystal defects [4–9]. These defects produce strongly spatially varying stress field in the surrounding lattice [10]. In the far-field approximation, defects can be treated as anisotropic point objects interacting with other defects through their elastic fields [11–18]. These fields generate forces and torques acting on the defects that drive their collec-

tive evolution [19]. This evolution changes microstructure of a material exposed to irradiation and has a significant effect on mechanical and physical properties [20].

Under continuous irradiation, defects accumulate and microstructure eventually reaches saturation, or adopts a gradually evolving structural state [19,21,22]. Transmission electron microscope (TEM) observations of ion irradiated Fe, Ni, and Cu [23] show that the rate of accumulation of defects in Fe is lower than in Ni and Cu. TEM experiments also show that the density of defect clusters in neutron irradiated molybdenum and its alloys is substantially lower than in copper, and that the difference is even larger at high irradiation temperature [24]. Singh and Evans [24] suggested that the size and the density of defect clusters produced in FCC metals is higher than in body-centered cubic (BCC) metals. Besides, defects in FCC metals are more likely to be sessile. This leads to greater radiation damage in FCC than in BCC metals.

A pure crystalline metal cannot accommodate exceedingly high density of defects. TEM experiments on neutron irradiated FCC copper, nickel, and aluminium suggest that the defect cluster density saturates at a several atomic percent level at the dose close to 0.1 dpa [25]. Recent atomic scale simulations on BCC tungsten [22] and iron [26] arrive at the same conclusion that at relatively low temperatures, the defect cluster density saturates at a dose close to 0.1 dpa. We note that both approaches [22,26] use the Frenkel pair insertion methodology, where an arbitrarily chosen atom is removed from the simulation cell and reinserted at a random position, followed by the atomic relaxation performed using a static [22] or a dynamic [26] algorithm. Each atomic removal and reinsertion increments the dose by $1/N$ dpa, where N is the total number of atoms in a simulation cell. Care should be taken when comparing simulations and observations, since

*leo.ma@ukaea.uk

Published by the American Physical Society under the terms of the [Creative Commons Attribution 4.0 International license](https://creativecommons.org/licenses/by/4.0/). Further distribution of this work must maintain attribution to the author(s) and the published article's title, journal citation, and DOI.

the above simulations do not treat atomic impacts or thermal spikes. Still, the approach is highly computationally efficient and enables reaching the dose of 20 dpa on a million-atom scale [22], predicting highly damaged microstructures similar to those observed experimentally [19].

The spatial resolution of a TEM is limited, and in a conventional imaging mode it is difficult to visualize point defects. For example, defects smaller than 1 nm in diameter can hardly be observed in a TEM [27–30]. Collision cascades simulations suggest that at doses not exceeding ~ 0.01 dpa, the frequency of occurrence of vacancy and interstitial defects of a certain size follows a power law [6–9]. This implies that a considerable fraction of defects is too small to be visible in a TEM.

To understand the dynamics of evolution of microstructure under irradiation and the effect of irradiation on properties, considerable effort is devoted to modeling and simulation of materials [31]. Object kinetic Monte Carlo (OKMC) simulations [32–34] are commonly applied to simulate the dynamics of evolution of irradiation-induced defects. These simulations are parameterized using input from *ab initio* calculations, molecular dynamics and atomic-scale kinetic Monte Carlo, which enable modeling diffusion, coalescence and dissociation, and recombination of defects. Although conventional OKMC methods often struggle to incorporate elastic interaction between the defects, some OKMC models successfully use the elastic dipole tensor formalism to describe interaction between defects, and enable evaluating effective sink strengths of interfaces [35] and dislocations [36], including effects of elastic interaction between point defects and interfaces/dislocations.

Derlet and Dudarev [22] showed that at relatively low temperatures, the evolution of microstructure is driven primarily by the spatially fluctuating stress fields associated with the defects. To correctly reproduce the morphology of evolving defect microstructure as a function of time, it is essential to treat elastic interactions between the defects. Defect dynamics models [37], based on a combination of the elastic dipole tensor and elastic Green's function treatment of elastic fields coupled to a finite element method solver, may provide a viable way of incorporating elastic interactions in a simulation of a relative low dose exposure of a material to irradiation under experimentally relevant conditions. While a general treatment of the high dose limit still appears elusive, the most recent results are encouraging [19].

The availability of high quality atomic-level input data remains the cornerstone aspect of the model development effort. Density functional theory (DFT) calculations enable extracting reliable information about the structure and elastic properties of localized defects from electronic and atomistic scale models, to enable mapping the results to a continuum linear elasticity model [10–18]. In this respect, DFT remains a powerful computational data-generating tool, providing information for materials modeling, consistent with experimental observations, at a reasonable computational cost [38].

A Frenkel pair is the most common defect produced in a material by irradiation [39]. It forms if an atom is displaced far away from its original lattice site, producing a vacancy at the original location, and a self-interstitial atom (SIA) defect. The atomic configuration of a vacancy is relatively simple and in most cases involves small relaxation of the near-neighbor

atoms towards the vacant lattice site. On the other hand, a SIA defect, forming if an extra atom is inserted in the lattice, often adopts a variety of fairly complex configurations.

In our previous studies [15–17], we examined the formation and migration energies and elastic dipole tensors of SIA and vacancy defects in almost all the body-centered cubic (BCC) metals. We have also evaluated the elastic correction to the defect formation energy associated with the use of periodic boundary conditions.

There is extensive literature on DFT analysis of monovacancies in FCC metals [40–65]. These studies extend beyond the treatment of static configurations and explore finite temperature scenarios through the use of the quasiharmonic approximation [53,54,58,60,64] and even include anharmonic contributions [65]. On the other hand, DFT calculations of formation and migration energies of SIA configurations are limited to Al [66,67] and Ni [68]. We also note a remarkable study of SIA configurations in Al performed using a many-body diffusion quantum Monte Carlo approach [69], a technique that is far more computationally demanding than DFT [70].

In this study, we perform DFT analysis of SIA defects in almost all the pure FCC metals. The study spans Al, Ca, Ni, Cu, Sr, Rh, Pd, Ag, Ir, Pt, Au, Pb, and Th. We evaluate formation energies of various high symmetry SIA and vacancy configurations, as well as elastic dipole and relaxation volume tensors of defects. The results form a comprehensive database of properties of defects required as input to continuum scale models [10]. We re-examine the long-standing assertion, based on x-ray diffraction data on Al, Cu, and Ni [71–73] that a $\langle 100 \rangle$ dumbbell represents the most stable SIA configuration in FCC metals. We find that this assertion is not universally applicable. The formation energies of other SIA configurations are close to, or even lower than that of the $\langle 100 \rangle$ dumbbell in several well-known FCC metals. We discuss implications of these results for the interpretation of observations of migration of SIA defects, comparing the new DFT results with a range of pertinent experimental data.

II. THEORY

The formation energy of a defect in a finite-size simulation cell computed using periodic boundary conditions equals [15–18]:

$$E_{\text{def}}^F = [E_{\text{def}}(N_{\text{def}}) - E^{\text{app}}] - \frac{N_{\text{def}}}{N_{\text{perf}}} E_{\text{perf}}(N_{\text{perf}}) - E_{\text{el}}^{\text{corr}}, \quad (1)$$

where E_{def} is the energy of a simulation cell containing a defect, E_{perf} is the energy of a perfect lattice cell representing a reference configuration, N_{def} is the number of atoms in the cell containing a defect, and N_{perf} is the number of atoms in a perfect lattice cell. E^{app} is the part of the total energy associated with externally applied strain, and $E_{\text{el}}^{\text{corr}}$ is the elastic correction energy that needs to be included to account for the effects of periodic boundary conditions. The energy associated with externally applied strain is

$$E^{\text{app}} = \frac{V_{\text{cell}}}{2} C_{ijkl} \epsilon_{ij}^{\text{app}} \epsilon_{kl}^{\text{app}} - P_{ij} \epsilon_{ij}^{\text{app}}, \quad (2)$$

where V_{cell} is the volume of the simulation cell. The applied strain $\epsilon_{ij}^{\text{app}}$ can be calculated from the cell vectors of the

TABLE I. The header of PAW potential, number of valence electrons (V. E.), and plane-wave energy cutoff of all elements being considered.

Element	Header of PAW potential	V. E.	Cutoff (eV)
Al	PAW_PBE Al 04Jan2001	3	400
Ca	PAW_PBE Ca_sv 06Sep2000	10	400
Ni	PAW_PBE Ni_pv 06Sep2000	16	600
Cu	PAW_PBE Cu 22Jun2005	11	600
Cu_pv	PAW_PBE Cu_pv 06Sep2000	17	600
Sr	PAW_PBE Sr_sv 07Sep2000	10	400
Rh	PAW_PBE Rh_pv 25Jan2005	15	400
Pd	PAW_PBE Pd_pv 28Jan2005	16	400
Ag	PAW_PBE Ag_pv 09Dec2005	17	450
Ir	PAW_PBE Ir 06Sep2000	9	350
Pt	PAW_PBE Pt 04Feb2005	10	450
Pt_pv	PAW_PBE Pt_pv 12Dec2005	16	450
Au	PAW_PBE Au 04Oct2007	11	450
Au_pv_GW	PAW Au_pv_GW 23Mar2010	17	450
Pb	PAW_PBE Pb 08Apr2002	4	400
Pb_d	PAW_PBE Pb_d 06Sep2000	14	400
Pb_d_GW	PAW Pb_d 06Oct2005	14	400
Th	PAW_PBE Th 07Sep2000	12	400

reference cell and the cell containing the defect. The elastic correction energy $E_{\text{el}}^{\text{corr}}$ also depends on the elastic dipole tensor P_{ij} of the defect. The elastic dipole tensor can be computed using the equation [12–15]

$$P_{ij} = V_{\text{cell}}(C_{ijkl}\epsilon_{kl}^{\text{app}} - \bar{\sigma}_{ij}), \quad (3)$$

where $\bar{\sigma}_{ij}$ is the average stress in the cell. The relaxation volume tensor can then be evaluated as

$$\Omega_{ij} = S_{ijkl}P_{kl}, \quad (4)$$

where S_{ijkl} is the elastic compliance tensor, satisfying the condition $C_{ijkl}S_{ikmn} = \frac{1}{2}(\delta_{im}\delta_{jn} + \delta_{in}\delta_{jm})$, where repeated indices imply summation. The relaxation volume of the defect is

$$\Omega^{\text{rel}} = \text{Tr}(\Omega_{ij}) = \Omega_{ii} = \Omega_{11} + \Omega_{22} + \Omega_{33}.$$

Further details related to the methods used for the evaluation of E^{app} , $E_{\text{el}}^{\text{corr}}$, P_{ij} , and Ω_{ij} can be found in Refs. [11–18]. A description of computer program CALANIE used for evaluating the above quantities is given in Ref. [18].

All the DFT calculations were performed using the Vienna *ab initio* simulation package (VASP) [74–77], version 5.4.1. We used a supercell containing $4 \times 4 \times 4$ FCC unit cells and $3 \times 3 \times 3$ k -point mesh. Each FCC unit cell contains four atoms. The selection of projector augmented-wave (PAW) potentials [78,79], provided by VASP, the number of valence electrons and the plane wave energy cutoff for different elements are summarized in Table I. For all the elements, we performed calculations using the GGA-PBE [80,81] exchange-correlation functional. We assumed that all metals were nonmagnetic, with the exception of nickel. Calculations for Ni were performed in the collinear magnetic approximation, assuming a collinear ferromagnetically ordered ground state. For some selected materials, including Cu, Ag, Ir, Pt, Au, Pb, and Th, we also performed calculations using the

GGA-PBEsol functional [82,83] with and without spin-orbit coupling.

We start by creating a perfect lattice simulation cell and relaxing it to the stress-free condition. Then, we create point defects by inserting or removing an atom from the simulation cell. We create various SIA defect configurations, including a $\langle 100 \rangle$ dumbbell, a $\langle 110 \rangle$ dumbbell, a $\langle 110 \rangle$ crowdion, a $\langle 111 \rangle$ dumbbell, a tetrahedral site interstitial and an octahedral site interstitial, as well as a vacancy configuration. The various SIA configurations considered in this work are illustrated in Fig. 1. Ion positions are then relaxed without altering the shape and the volume of the simulation cell. The convergence condition is defined by the maximum force acting on an atom in the cell, which was set to be lower than $0.01 \text{ eV}/\text{\AA}$.

For gold (Au), we have also performed calculations using the revised-TPSS exchange-correlation functional [84,85] that includes spin-orbit coupling. The inclusion of spin-orbit coupling is intended to account for the band splitting and shape modification of the $5d$ bands [86–88], where relativistic effects are significant. Some results derived from this analysis were presented earlier [18]. We use simulation cells with various shape and size for different defect configurations to optimize the computational effort that otherwise is associated with the uniform use of a relatively large simulation cell. The simulation cells used for analyzing various configurations of defects are listed in Table II.

The formation energies of defects were also computed by means of full relaxation to the stress-free condition, using cells of similar size with the same k -point sampling. The resulting formation energies, evaluated using Eq. (1) and including the appropriate elastic corrections, were virtually identical to those computed using the fixed cell approach, also with the corresponding elastic corrections [15].

Although it might appear natural to introduce strong on-site Coulomb electron-electron repulsion in the treatment of f electrons in thorium (Th), it is known that the GGA-PBE treatment of correlations reproduces the lattice constant of ThO_2 well even if the effective Hubbard parameter U is set to zero [89]. Our calculations also show that the equilibrium lattice parameter and elastic constants of pure Th match experimental observations well.

The magnitude of spin-orbit coupling increases rapidly as a function of atomic number, since the spin-orbit coupling constant is proportional to the square of atomic number Z [90]. Therefore we include spin-orbit coupling in the simulations of defects in heavy elements, including Ir, Pt, Au, Pb, and Th. When performing calculations for Cu and Ag, we include the treatment of spin-orbit coupling because they are in the same group as Au.

The use of PBEsol [82,83] exchange-correlation functional is justified by the need to reduce the discrepancy between the vacancy formation energy E_V^f predicted by DFT calculations and that found in experiment. Because of the same reason, we use meta-GGA rTPSS [84] when investigating defects in gold. The relevant numerical values are discussed in the next section of the paper. PBEsol was developed to correct the surface energy by restoring the second-order gradient expansion for exchange over a wide range of densities [82,83]. The rTPSS [84] was revised from TPSS [91] following the same principles for the purpose of obtaining better values for the

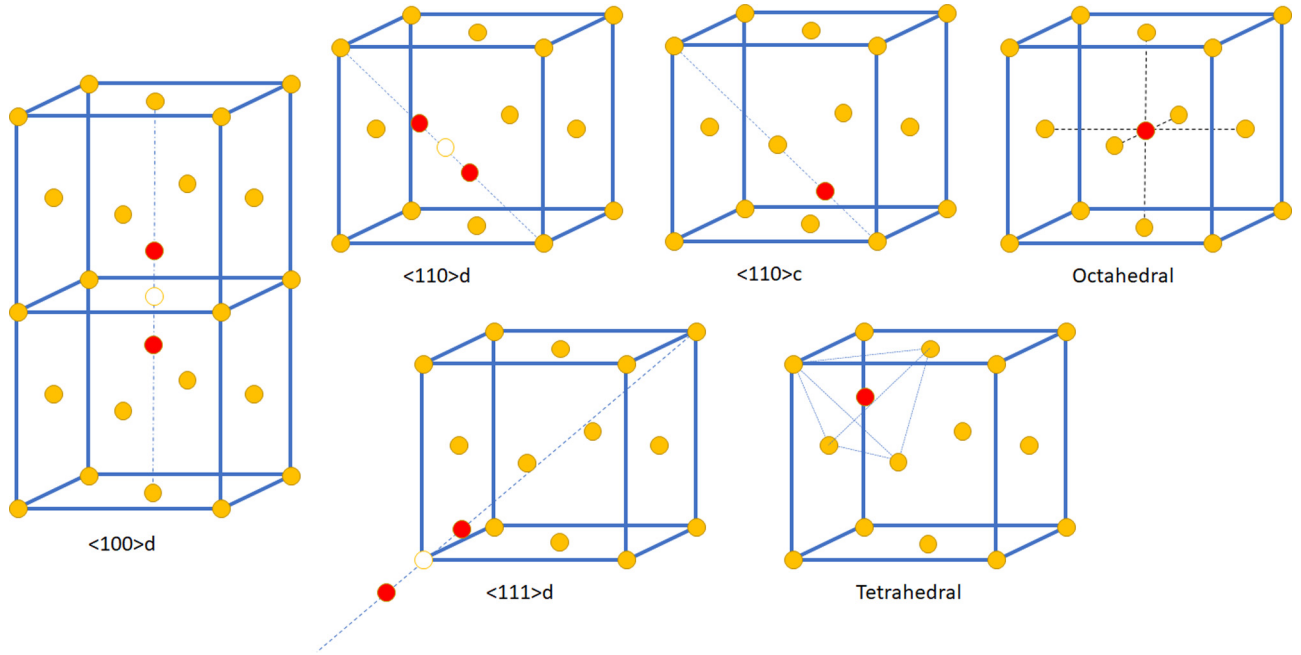


FIG. 1. Schematic sketches of self-interstitial atom defect structures in face-centered cubic metals. In all the cases illustrated in this figure, a simulation cell contains one extra atom, and hence the corresponding atomic configuration represents a single-atom SIA defect. All the atoms shown in the sketches are identical, and colors highlight the symmetry of a particular defect structure. Empty spheres, where appropriate, indicate positions of unoccupied ideal lattice sites. Letters d or c refer to a dumbbell or crowdion configuration.

lattice constant, while keeping the surface and atomization energies unaffected. Both rTPSS and TPSS are semilocal functionals that include the kinetic energy density.

Ropo *et al.* [92] examined surface energies of various metals, and showed that calculations using the PBEsol functional predict significantly higher surface energies than calculations using the PBE functional. Medasani *et al.* [93] examined the trend of E_V^F for a set of 34 metals. They found that the magnitude of E_V^F generally follows the trend rTPSS > PBEsol \approx LDA > PBE > PW91, where rTPSS, PBEsol, and LDA lead to better overall agreement with experiment.

We would like to highlight the work by Glensk *et al.* [65] who suggested that the discrepancy between the vacancy formation free energy found in DFT calculations and values derived from positron annihilation spectroscopy or differential dilatometry at high temperature might be due to the temper-

ature dependent entropy term. They developed a technique to sample anharmonic contribution to the free energy within the framework of DFT. The calculated vacancy formation free energies in Al and Cu showed that the results obtained using the PBE functional were in better agreement with experiment than those obtained using the AM05 and surface-corrected PW91 functionals. This indicated that adding surface energy correction either by modifying the exchange-correlation functional or as post-processing might not be necessary if anharmonic contribution is taken into account. A comprehensive study of the formation free energies of defects using various exchange-correlation functional and including anharmonic contributions is desirable, but at present, it is outside the scope of this study.

In order to evaluate the contribution to energy associated with applied strain E^{app} , the elastic correction energy $E_{\text{el}}^{\text{corr}}$, and the relaxation volume tensor Ω_{ij} , it is necessary to compute the full tensor of elastic constants. In this study, the elastic constant tensors C_{ijkl} were evaluated for all the metals using the Le Page and Saxe method [94] using a four-atom cubic simulation cell and a $21 \times 21 \times 21$ k -point mesh. The atomic volume Ω_0 and the equilibrium lattice constant a_0 were also determined from the same set of calculations. However, when converting Ω_{ij} into the Ω_0 units, we used the volume of the supercell representing the reference crystal structure for a defect calculation. The results are summarized in Table III together with the relevant experimental data. The predicted values are generally in agreement with experiment.

III. NUMERICAL RESULTS

Formation energies of defects E^F , elements of elastic dipole tensors P_{ij} and relaxation volume tensors Ω_{ij} ,

TABLE II. Number of atoms, approximate cell size (in units of the unit cell size), and the k -point mesh used in the calculations of SIA and vacancy configurations in FCC gold (Au).

	No. of atoms	Approx. cell size	k points
<100>d	145	$3 \times 3 \times 4$	$4 \times 4 \times 3$
Octa	109	$3 \times 3 \times 3$	$4 \times 4 \times 4$
<110>c	193	$3 \times 4 \times 4$	$4 \times 3 \times 3$
<110>d	193	$3 \times 4 \times 4$	$4 \times 3 \times 3$
<111>d	109	$3 \times 3 \times 3$	$4 \times 4 \times 4$
Tetra	109	$3 \times 3 \times 3$	$4 \times 4 \times 4$
Vac	107	$3 \times 3 \times 3$	$4 \times 4 \times 4$

TABLE III. Calculated elastic constants C_{ij} , lattice constants a , atomic volume Ω_0 , vacancy formation energy E_V^F and the most stable SIA formation energy E_{SIA}^F . Experimental data for elastic constants are taken from Ref. [110]. Experimentally observed values of lattice constants are taken from Ref. [97], with the exception of Ca and Sr, where they are taken from Ref. [111]. Experimental data for vacancy and SIA formation energies are taken from Ref. [97].

Element	Functional	C_{11} (GPa)	C_{12} (GPa)	C_{44} (GPa)	a (Å)	Ω_0 (Å ³)	E_V^F (eV)	E_{SIA}^F (eV)
Al	Experiment	108	62	28	4.050	16.603	0.67 ± 0.03	3.0
Al	PBE	100.307	64.316	23.565	4.040	16.486	0.638	2.587
Ca	Experiment	22.8/27.8	16.0/18.2	14/16.3	5.58	43.435	–	–
Ca	PBE	22.234	14.853	13.564	5.527	42.220	1.156	1.902
Ni	Experiment	247	153	122	3.524	10.939	1.79 ± 0.05	–
Ni	PBE	298.190	165.749	138.156	3.511	10.818	1.447	4.493
Cu	Experiment	169	122	75	3.615	11.813	1.28 ± 0.05	2.82 to 4.12
Cu	PBE	178.484	129.262	74.128	3.634	12.000	1.064	3.088
Cu_pv	PBE	201.507	131.304	85.442	3.622	11.874	1.059	3.379
Cu	PBEsol	205.307	139.194	88.035	3.568	11.355	1.224	3.433
Cu_pv	PBEsol	226.394	144.724	91.916	3.559	11.270	1.269	3.766
Cu	PBEsol+SOC	211.015	145.872	84.418	3.568	11.360	1.222	3.438
Cu_pv	PBEsol+SOC	230.224	145.099	91.751	3.559	11.266	1.264	3.768
Sr	Experiment	15.3	10.3	9.9	6.08	56.189	–	–
Sr	PBE	14.623	10.062	9.220	6.018	54.489	1.045	2.053
Rh	Experiment	413	194	184	3.804	13.757	–	–
Rh	PBE	430.323	183.901	192.399	3.823	13.968	1.873	6.735
Pd	Experiment	221	171	70.8	3.891	14.725	1.70/1.85	–
Pd	PBE	215.890	162.613	63.934	3.930	15.177	1.306	4.454
Ag	Experiment	122	92	45.5	4.086	17.058	1.11 ± 0.05	–
Ag	PBE	126.343	97.736	44.049	4.121	17.495	0.711	3.238
Ag	PBEsol	154.105	118.540	51.357	4.037	16.444	1.155	3.929
Ag	PBEsol+SOC	153.880	117.667	51.580	4.037	16.443	1.152	3.927
Ir	Experiment	600/580	270/256	260/242	3.839	14.144	–	–
Ir	PBE	616.979	242.793	273.587	3.859	14.363	1.519	8.687
Ir	PBEsol	650.965	264.366	286.970	3.833	14.073	1.979	9.617
Ir	PBEsol+SOC	637.776	257.173	276.575	3.836	14.108	1.779	9.232
Pt	Experiment	347	251	76.5	3.924	15.105	1.35 ± 0.05	1.7
Pt	PBE	309.303	218.239	59.590	3.968	15.614	0.545	4.825
Pt_pv	PBE	344.308	232.445	69.481	3.959	15.514	0.458	5.285
Pt	PBEsol	363.316	252.130	76.510	3.917	15.019	0.785	5.557
Pt	PBEsol+SOC	355.641	247.011	80.443	3.919	15.045	0.831	5.501
Au	Experiment	191	162	42.2	4.078	16.958	0.93 ± 0.04	–
Au	PBE	145.366	135.479	21.978	4.157	17.963	0.442	2.602
Au_pv_GW	PBE	154.975	138.733	22.963	4.160	17.991	0.418	2.683
Au	PBEsol	193.950	167.045	32.891	4.082	17.000	0.765	3.374
Au	PBEsol+SOC	202.004	169.796	36.051	4.072	16.878	0.662	3.369
Au	RTPSS+SOC	210.550	168.107	49.964	4.075	16.920	0.939	3.938
Pb	Experiment	48.8	41.4	14.8	4.950	30.322	0.58 ± 0.04	–
Pb	PBE	50.238	36.107	19.880	5.028	31.770	0.299	1.254
Pb_d	PBE	54.393	36.481	21.749	5.036	31.938	0.285	1.295
Pb_d_GW	PBE	49.737	35.321	20.949	5.036	31.937	0.279	1.285
Pb	PBSol	52.722	43.352	13.863	4.930	29.947	0.407	1.365
Pb	PBEsol+SOC	59.142	39.724	24.470	4.934	30.031	0.295	0.987
Th	Experiment	75.3/77.0	48.9/50.9	47.8/45.5	5.084	32.855	1.28 ± 0.2	–
Th	PBE	86.475	39.921	57.434	5.054	32.282	2.444	4.802
Th	PBEsol	89.784	45.847	63.600	4.959	30.481	2.668	5.270
Th	PBEsol+SOC	94.630	47.875	63.791	4.933	30.012	2.458	5.159

as well as relaxation volumes Ω^{rel} computed for vacancy and various SIA configurations are summarized in Tables IV to XXXVIII. Formation energies of the most stable SIA and vacancy configurations are also given in Table III.

A. Vacancies

Vacancy formation energies E_V^F computed in this study for FCC metals are generally compatible with experimental values, and agree with recent DFT calculations by Medasani *et al.* [93], Angsten *et al.* [59], and Nazarov *et al.* [57].

TABLE IV. Formation energy of a defect E^F (in eV units), elements of its dipole tensor P_{ij} (in eV units), and relaxation volume tensor Ω_{ij} (in Ω_0 units), as well as the relaxation volume of a defect Ω^{rel} (in Ω_0 units) computed for Al using the GGA-PBE functional.

Al	E^F	P_{11}	P_{22}	P_{33}	P_{12}	P_{23}	P_{31}	Ω_{11}	Ω_{22}	Ω_{33}	Ω_{12}	Ω_{23}	Ω_{31}	Ω^{rel}
$\langle 100 \rangle$ d	2.587	17.399	18.376	18.376	0.000	0.000	0.000	0.591	0.855	0.855	0.000	0.000	0.000	2.301
Octa	2.812	18.873	18.873	18.873	0.000	0.000	0.000	0.802	0.802	0.802	0.000	0.000	0.000	2.406
$\langle 110 \rangle$ c	2.902	18.418	18.418	21.165	11.753	0.000	0.000	0.574	0.574	1.316	2.426	0.000	0.000	2.465
$\langle 110 \rangle$ d	2.902	18.440	18.440	21.127	11.768	0.000	0.000	0.580	0.580	1.306	2.429	0.000	0.000	2.465
$\langle 111 \rangle$ d	3.083	19.657	19.657	19.657	3.021	3.021	3.021	0.835	0.835	0.835	0.624	0.624	0.624	2.506
Tetra	3.118	19.847	19.847	19.847	0.000	0.000	0.000	0.843	0.843	0.843	0.000	0.000	0.000	2.530
Vac	0.638	-1.911	-1.911	-1.911	0.000	0.000	0.000	-0.081	-0.081	-0.081	0.000	0.000	0.000	-0.244

TABLE V. Formation energy of a defect E^F (in eV units), elements of its dipole tensor P_{ij} (in eV units), and relaxation volume tensor Ω_{ij} (in Ω_0 units), as well as the relaxation volume of a defect Ω^{rel} (in Ω_0 units) computed for Ca using the GGA-PBE functional.

Ca	E^F	P_{11}	P_{22}	P_{33}	P_{12}	P_{23}	P_{31}	Ω_{11}	Ω_{22}	Ω_{33}	Ω_{12}	Ω_{23}	Ω_{31}	Ω^{rel}
$\langle 100 \rangle$ d	1.902	6.464	6.398	6.398	0.000	0.000	0.000	0.492	0.458	0.458	0.000	0.000	0.000	1.408
Octa	2.171	6.444	6.444	6.444	0.000	0.000	0.000	0.471	0.471	0.471	0.000	0.000	0.000	1.413
$\langle 110 \rangle$ c	1.995	5.129	5.129	7.541	4.716	0.000	0.000	0.020	0.020	1.261	0.660	0.000	0.000	1.301
$\langle 110 \rangle$ d	1.995	5.123	5.123	7.536	4.717	0.000	0.000	0.020	0.020	1.261	0.660	0.000	0.000	1.300
$\langle 111 \rangle$ d	2.097	6.216	6.216	6.216	2.390	2.390	2.390	0.454	0.454	0.454	0.334	0.334	0.334	1.363
Tetra	2.156	6.321	6.321	6.321	0.000	0.000	0.000	0.462	0.462	0.462	0.000	0.000	0.000	1.386
Vac	1.156	-1.068	-1.068	-1.068	0.000	0.000	0.000	-0.078	-0.078	-0.078	0.000	0.000	0.000	-0.234

TABLE VI. Formation energy of a defect E^F (in eV units), elements of its dipole tensor P_{ij} (in eV units), and relaxation volume tensor Ω_{ij} (in Ω_0 units), as well as the relaxation volume of a defect Ω^{rel} (in Ω_0 units) computed for Ni using the GGA-PBE functional.

Ni	E^F	P_{11}	P_{22}	P_{33}	P_{12}	P_{23}	P_{31}	Ω_{11}	Ω_{22}	Ω_{33}	Ω_{12}	Ω_{23}	Ω_{31}	Ω^{rel}
$\langle 100 \rangle$ d	4.493	25.668	25.237	25.237	0.000	0.000	0.000	0.629	0.581	0.581	0.000	0.000	0.000	1.792
Octa	4.714	26.097	26.097	26.097	0.000	0.000	0.000	0.614	0.614	0.614	0.000	0.000	0.000	1.842
$\langle 110 \rangle$ c	5.281	25.140	25.140	29.074	15.623	0.000	0.000	0.476	0.476	0.916	0.838	0.000	0.000	1.867
$\langle 110 \rangle$ d	5.282	25.124	25.124	29.097	15.615	0.000	0.000	0.474	0.474	0.919	0.837	0.000	0.000	1.867
$\langle 111 \rangle$ d	5.109	26.412	26.412	26.412	2.333	2.333	2.333	0.621	0.621	0.621	0.125	0.125	0.125	1.864
Tetra	5.093	26.441	26.441	26.441	0.000	0.000	0.000	0.622	0.622	0.622	0.000	0.000	0.000	1.866
Vac	1.447	-5.067	-5.067	-5.067	0.000	0.000	0.000	-0.119	-0.119	-0.119	0.000	0.000	0.000	-0.358

TABLE VII. Formation energy of a defect E^F (in eV units), elements of its dipole tensor P_{ij} (in eV units), and relaxation volume tensor Ω_{ij} (in Ω_0 units), as well as the relaxation volume of a defect Ω^{rel} (in Ω_0 units) computed for Cu using the GGA-PBE functional.

Cu	E^F	P_{11}	P_{22}	P_{33}	P_{12}	P_{23}	P_{31}	Ω_{11}	Ω_{22}	Ω_{33}	Ω_{12}	Ω_{23}	Ω_{31}	Ω^{rel}
$\langle 100 \rangle$ d	3.088	19.448	19.198	19.198	0.000	0.000	0.000	0.634	0.566	0.566	0.000	0.000	0.000	1.767
Octa	3.352	20.000	20.000	20.000	0.000	0.000	0.000	0.611	0.611	0.611	0.000	0.000	0.000	1.832
$\langle 110 \rangle$ c	3.386	19.011	19.011	21.629	11.980	0.000	0.000	0.371	0.371	1.080	1.078	0.000	0.000	1.822
$\langle 110 \rangle$ d	3.386	19.017	19.017	21.626	11.968	0.000	0.000	0.372	0.372	1.079	1.077	0.000	0.000	1.822
$\langle 111 \rangle$ d	3.593	20.154	20.154	20.154	3.797	3.797	3.797	0.616	0.616	0.616	0.342	0.342	0.342	1.847
Tetra	3.644	20.187	20.187	20.187	0.000	0.000	0.000	0.617	0.617	0.617	0.000	0.000	0.000	1.850
Vac	1.064	-3.940	-3.940	-3.940	0.000	0.000	0.000	-0.120	-0.120	-0.120	0.000	0.000	0.000	-0.361

TABLE VIII. Formation energy of a defect E^F (in eV units), elements of its dipole tensor P_{ij} (in eV units), and relaxation volume tensor Ω_{ij} (in Ω_0 units), as well as the relaxation volume of a defect Ω^{rel} (in Ω_0 units) computed for Cu_pv using the GGA-PBE functional.

Cu_pv	E^F	P_{11}	P_{22}	P_{33}	P_{12}	P_{23}	P_{31}	Ω_{11}	Ω_{22}	Ω_{33}	Ω_{12}	Ω_{23}	Ω_{31}	Ω_{rel}
$\langle 100 \rangle$ d	3.379	20.453	20.454	20.454	0.000	0.000	0.000	0.596	0.596	0.596	0.000	0.000	0.000	1.787
Octa	3.657	21.242	21.242	21.242	0.000	0.000	0.000	0.619	0.619	0.619	0.000	0.000	0.000	1.856
$\langle 110 \rangle$ c	3.700	20.050	20.050	23.199	12.328	0.000	0.000	0.412	0.412	1.019	0.975	0.000	0.000	1.844
$\langle 110 \rangle$ d	3.700	20.060	20.060	23.186	12.333	0.000	0.000	0.414	0.414	1.016	0.976	0.000	0.000	1.844
$\langle 111 \rangle$ d	3.907	21.453	21.453	21.453	3.958	3.958	3.958	0.625	0.625	0.625	0.313	0.313	0.313	1.875
Tetra	3.954	21.398	21.398	21.398	0.000	0.000	0.000	0.623	0.623	0.623	0.000	0.000	0.000	1.870
Vac	1.059	-3.729	-3.729	-3.729	0.000	0.000	0.000	-0.109	-0.109	-0.109	0.000	0.000	0.000	-0.326

TABLE IX. Formation energy of a defect E^F (in eV units), elements of its dipole tensor P_{ij} (in eV units), and relaxation volume tensor Ω_{ij} (in Ω_0 units), as well as the relaxation volume of a defect Ω^{rel} (in Ω_0 units) computed for Cu using the GGA-PBESol functional.

Cu	E^F	P_{11}	P_{22}	P_{33}	P_{12}	P_{23}	P_{31}	Ω_{11}	Ω_{22}	Ω_{33}	Ω_{12}	Ω_{23}	Ω_{31}	Ω_{rel}
$\langle 100 \rangle$ d	3.433	21.673	22.040	22.040	0.000	0.000	0.000	0.587	0.665	0.665	0.000	0.000	0.000	1.917
Octa	3.733	22.725	22.725	22.725	0.000	0.000	0.000	0.662	0.662	0.662	0.000	0.000	0.000	1.987
$\langle 110 \rangle$ c	3.768	21.312	21.312	25.090	12.846	0.000	0.000	0.389	0.389	1.195	1.029	0.000	0.000	1.974
$\langle 110 \rangle$ d	3.768	21.318	21.318	25.053	12.854	0.000	0.000	0.392	0.392	1.189	1.029	0.000	0.000	1.973
$\langle 111 \rangle$ d	3.990	22.836	22.836	22.836	4.082	4.082	4.082	0.666	0.666	0.666	0.327	0.327	0.327	1.997
Tetra	4.042	22.900	22.900	22.900	0.000	0.000	0.000	0.668	0.668	0.668	0.000	0.000	0.000	2.003
Vac	1.224	-3.794	-3.794	-3.794	0.000	0.000	0.000	-0.111	-0.111	-0.111	0.000	0.000	0.000	-0.332

TABLE X. Formation energy of a defect E^F (in eV units), elements of its dipole tensor P_{ij} (in eV units), and relaxation volume tensor Ω_{ij} (in Ω_0 units), as well as the relaxation volume of a defect Ω^{rel} (in Ω_0 units) computed for Cu_pv using the GGA-PBESol functional.

Cu_pv	E^F	P_{11}	P_{22}	P_{33}	P_{12}	P_{23}	P_{31}	Ω_{11}	Ω_{22}	Ω_{33}	Ω_{12}	Ω_{23}	Ω_{31}	Ω_{rel}
$\langle 100 \rangle$ d	3.766	22.995	23.663	23.663	0.000	0.000	0.000	0.570	0.687	0.687	0.000	0.000	0.000	1.944
Octa	4.079	24.201	24.201	24.201	0.000	0.000	0.000	0.669	0.669	0.669	0.000	0.000	0.000	2.007
$\langle 110 \rangle$ c	4.121	22.537	22.537	27.080	13.140	0.000	0.000	0.400	0.400	1.194	1.019	0.000	0.000	1.994
$\langle 110 \rangle$ d	4.120	22.627	22.627	27.058	13.121	0.000	0.000	0.408	0.408	1.182	1.018	0.000	0.000	1.999
$\langle 111 \rangle$ d	4.347	24.351	24.351	24.351	3.835	3.835	3.835	0.673	0.673	0.673	0.297	0.297	0.297	2.019
Tetra	4.393	24.576	24.576	24.576	0.000	0.000	0.000	0.679	0.679	0.679	0.000	0.000	0.000	2.038
Vac	1.269	-3.177	-3.177	-3.177	0.000	0.000	0.000	-0.088	-0.088	-0.088	0.000	0.000	0.000	-0.263

TABLE XI. Formation energy of a defect E^F (in eV units), elements of its dipole tensor P_{ij} (in eV units), and relaxation volume tensor Ω_{ij} (in Ω_0 units), as well as the relaxation volume of a defect Ω^{rel} (in Ω_0 units) computed for Cu using the GGA-PBESol functional with spin-orbit coupling.

Cu	E^F	P_{11}	P_{22}	P_{33}	P_{12}	P_{23}	P_{31}	Ω_{11}	Ω_{22}	Ω_{33}	Ω_{12}	Ω_{23}	Ω_{31}	Ω_{rel}
$\langle 100 \rangle$ d	3.438	21.509	21.911	21.911	0.000	0.000	0.000	0.553	0.640	0.640	0.000	0.000	0.000	1.833
Octa	3.739	22.728	22.728	22.728	0.000	0.000	0.000	0.638	0.638	0.638	0.000	0.000	0.000	1.913
$\langle 110 \rangle$ c	3.773	21.305	21.305	24.973	12.903	0.000	0.000	0.367	0.367	1.161	1.078	0.004	0.004	1.896
$\langle 110 \rangle$ d	3.774	21.176	21.176	24.831	12.917	0.000	0.000	0.364	0.364	1.156	1.079	0.004	0.004	1.885
$\langle 111 \rangle$ d	3.995	22.806	22.806	22.806	4.131	4.131	4.131	0.640	0.640	0.640	0.347	0.347	0.347	1.919
Tetra	4.048	22.860	22.860	22.860	0.000	0.000	0.000	0.641	0.641	0.641	0.000	0.000	0.000	1.924
Vac	1.222	-3.965	-3.965	-3.965	0.000	0.000	0.000	-0.111	-0.111	-0.111	0.000	0.000	0.000	-0.334

TABLE XII. Formation energy of a defect E^F (in eV units), elements of its dipole tensor P_{ij} (in eV units), and relaxation volume tensor Ω_{ij} (in Ω_0 units), as well as the relaxation volume of a defect Ω^{rel} (in Ω_0 units) computed for Cu_pv using GGA-PBESol functional and with spin-orbit coupling.

Cu_pv	E^F	P_{11}	P_{22}	P_{33}	P_{12}	P_{23}	P_{31}	Ω_{11}	Ω_{22}	Ω_{33}	Ω_{12}	Ω_{23}	Ω_{31}	Ω_{rel}
$\langle 100 \rangle$ d	3.768	22.967	23.628	23.628	0.000	0.000	0.000	0.567	0.678	0.678	0.000	0.000	0.000	1.924
Octa	4.080	24.116	24.116	24.116	0.000	0.000	0.000	0.661	0.661	0.661	0.000	0.000	0.000	1.982
$\langle 110 \rangle$ c	4.124	22.399	22.401	26.935	13.095	0.000	0.000	0.402	0.402	1.162	1.017	0.000	0.000	1.965
$\langle 110 \rangle$ d	4.124	22.518	22.518	26.947	13.026	0.000	0.000	0.410	0.410	1.152	1.012	0.000	0.000	1.972
$\langle 111 \rangle$ d	4.347	24.560	24.560	24.560	3.829	3.829	3.829	0.673	0.673	0.673	0.298	0.298	0.298	2.019
Tetra	4.395	24.441	24.441	24.441	0.000	0.000	0.000	0.670	0.670	0.670	0.000	0.000	0.000	2.009
Vac	1.264	-3.617	-3.617	-3.617	0.000	0.000	0.000	-0.099	-0.099	-0.099	0.000	0.000	0.000	-0.297

TABLE XIII. Formation energy of a defect E^F (in eV units), elements of its dipole tensor P_{ij} (in eV units), and relaxation volume tensor Ω_{ij} (in Ω_0 units), as well as the relaxation volume of a defect Ω^{rel} (in Ω_0 units) computed for Sr using GGA-PBE functional.

Sr	E^F	P_{11}	P_{22}	P_{33}	P_{12}	P_{23}	P_{31}	Ω_{11}	Ω_{22}	Ω_{33}	Ω_{12}	Ω_{23}	Ω_{31}	Ω^{rel}
$\langle 100 \rangle$ d	2.053	6.906	7.430	7.430	0.000	0.000	0.000	0.389	0.727	0.727	0.000	0.000	0.000	1.843
Octa	2.348	6.998	6.998	6.998	0.000	0.000	0.000	0.592	0.592	0.592	0.000	0.000	0.000	1.777
$\langle 110 \rangle$ c	2.069	5.746	5.746	8.086	6.797	0.000	0.000	0.049	0.049	1.559	1.084	0.000	0.000	1.657
$\langle 110 \rangle$ d	2.069	5.748	5.748	8.080	6.795	0.000	0.000	0.051	0.051	1.555	1.084	0.000	0.000	1.657
$\langle 111 \rangle$ d	2.227	6.851	6.851	6.851	3.742	3.742	3.742	0.580	0.580	0.580	0.597	0.597	0.597	1.740
Tetra	2.365	7.079	7.079	7.079	0.000	0.000	0.000	0.599	0.599	0.599	0.000	0.000	0.000	1.798
Vac	1.045	-0.832	-0.832	-0.832	0.000	0.000	0.000	-0.070	-0.070	-0.070	0.000	0.000	0.000	-0.211

TABLE XIV. Formation energy of a defect E^F (in eV units), elements of its dipole tensor P_{ij} (in eV units), and relaxation volume tensor Ω_{ij} (in Ω_0 units), as well as the relaxation volume of a defect Ω^{rel} (in Ω_0 units) computed for Rh using GGA-PBE functional.

Rh	E^F	P_{11}	P_{22}	P_{33}	P_{12}	P_{23}	P_{31}	Ω_{11}	Ω_{22}	Ω_{33}	Ω_{12}	Ω_{23}	Ω_{31}	Ω^{rel}
$\langle 100 \rangle$ d	6.859	42.374	47.121	47.121	0.000	0.000	0.000	0.507	0.728	0.728	0.000	0.000	0.000	1.963
Octa	6.735	46.103	46.103	46.103	0.000	0.000	0.000	0.663	0.663	0.663	0.000	0.000	0.000	1.988
$\langle 110 \rangle$ c	8.489	46.917	46.917	49.265	21.825	0.000	0.000	0.649	0.649	0.758	0.651	0.000	0.000	2.057
$\langle 110 \rangle$ d	8.493	46.967	46.967	49.183	21.849	0.000	0.000	0.651	0.651	0.754	0.651	0.000	0.000	2.057
$\langle 111 \rangle$ d	7.751	48.170	48.170	48.170	-0.997	-0.997	-0.997	0.692	0.692	0.692	-0.030	-0.030	-0.030	2.077
Tetra	7.665	47.627	47.627	47.627	0.000	0.000	0.000	0.685	0.685	0.685	0.000	0.000	0.000	2.054
Vac	1.873	-8.756	-8.756	-8.756	0.000	0.000	0.000	-0.126	-0.126	-0.126	0.000	0.000	0.000	-0.378

TABLE XV. Formation energy of a defect E^F (in eV units), elements of its dipole tensor P_{ij} (in eV units), and relaxation volume tensor Ω_{ij} (in Ω_0 units), as well as the relaxation volume of a defect Ω^{rel} (in Ω_0 units) computed for Pd using GGA-PBE functional.

Pd	E^F	P_{11}	P_{22}	P_{33}	P_{12}	P_{23}	P_{31}	Ω_{11}	Ω_{22}	Ω_{33}	Ω_{12}	Ω_{23}	Ω_{31}	Ω^{rel}
$\langle 100 \rangle$ d	4.454	29.811	32.267	32.267	0.000	0.000	0.000	0.289	0.774	0.774	0.000	0.000	0.000	1.836
Octa	4.644	32.256	32.256	32.256	0.000	0.000	0.000	0.628	0.628	0.628	0.000	0.000	0.000	1.884
$\langle 110 \rangle$ c	4.743	31.937	31.937	33.327	12.810	0.000	0.000	0.539	0.539	0.814	1.055	0.000	0.000	1.892
$\langle 110 \rangle$ d	4.743	31.942	31.942	33.315	12.816	0.000	0.000	0.540	0.540	0.812	1.056	0.000	0.000	1.892
$\langle 111 \rangle$ d	4.884	32.493	32.493	32.493	2.564	2.564	2.564	0.632	0.632	0.632	0.211	0.211	0.211	1.897
Tetra	5.062	32.842	32.842	32.842	0.000	0.000	0.000	0.639	0.639	0.639	0.000	0.000	0.000	1.918
Vac	1.306	-7.361	-7.361	-7.361	0.000	0.000	0.000	-0.143	-0.143	-0.143	0.000	0.000	0.000	-0.430

TABLE XVI. Formation energy of a defect E^F (in eV units), elements of its dipole tensor P_{ij} (in eV units), and relaxation volume tensor Ω_{ij} (in Ω_0 units), as well as the relaxation volume of a defect Ω^{rel} (in Ω_0 units) computed for Ag using GGA-PBE functional.

Ag	E^F	P_{11}	P_{22}	P_{33}	P_{12}	P_{23}	P_{31}	Ω_{11}	Ω_{22}	Ω_{33}	Ω_{12}	Ω_{23}	Ω_{31}	Ω^{rel}
$\langle 100 \rangle$ d	3.238	21.611	22.367	22.367	0.000	0.000	0.000	0.468	0.711	0.711	0.000	0.000	0.000	1.890
Octa	3.403	22.785	22.785	22.785	0.000	0.000	0.000	0.649	0.649	0.649	0.000	0.000	0.000	1.947
$\langle 110 \rangle$ c	3.433	22.015	22.015	24.048	10.313	0.000	0.000	0.429	0.429	1.081	1.073	0.000	0.000	1.939
$\langle 110 \rangle$ d	3.433	22.016	22.016	24.053	10.311	0.000	0.000	0.429	0.429	1.081	1.073	0.000	0.000	1.939
$\langle 111 \rangle$ d	3.741	23.275	23.275	23.275	2.960	2.960	2.960	0.663	0.663	0.663	0.308	0.308	0.308	1.989
Tetra	3.799	23.392	23.392	23.392	0.000	0.000	0.000	0.666	0.666	0.666	0.000	0.000	0.000	1.999
Vac	0.711	-3.015	-3.015	-3.015	0.000	0.000	0.000	-0.086	-0.086	-0.086	0.000	0.000	0.000	-0.258

TABLE XVII. Formation energy of a defect E^F (in eV units), elements of its dipole tensor P_{ij} (in eV units), and relaxation volume tensor Ω_{ij} (in Ω_0 units), as well as the relaxation volume of a defect Ω^{rel} (in Ω_0 units) computed for Ag using GGA-PBEsol functional.

Ag	E^F	P_{11}	P_{22}	P_{33}	P_{12}	P_{23}	P_{31}	Ω_{11}	Ω_{22}	Ω_{33}	Ω_{12}	Ω_{23}	Ω_{31}	Ω^{rel}
$\langle 100 \rangle$ d	3.929	26.457	27.129	27.129	0.000	0.000	0.000	0.549	0.734	0.734	0.000	0.000	0.000	2.017
Octa	4.117	27.697	27.697	27.697	0.000	0.000	0.000	0.692	0.692	0.692	0.000	0.000	0.000	2.076
$\langle 110 \rangle$ c	4.134	26.844	26.844	29.062	12.965	0.000	0.000	0.486	0.486	1.096	1.234	0.000	0.000	2.068
$\langle 110 \rangle$ d	4.135	26.850	26.850	29.032	12.921	0.000	0.000	0.489	0.489	1.089	1.230	0.000	0.000	2.067
$\langle 111 \rangle$ d	4.500	28.228	28.228	28.228	4.036	4.036	4.036	0.705	0.705	0.705	0.384	0.384	0.384	2.116
Tetra	4.572	28.306	28.306	28.306	0.000	0.000	0.000	0.707	0.707	0.707	0.000	0.000	0.000	2.122
Vac	1.155	-3.924	-3.924	-3.924	0.000	0.000	0.000	-0.098	-0.098	-0.098	0.000	0.000	0.000	-0.294

TABLE XVIII. Formation energy of a defect E^F (in eV units), elements of its dipole tensor P_{ij} (in eV units), and relaxation volume tensor Ω_{ij} (in Ω_0 units), as well as the relaxation volume of a defect Ω^{rel} (in Ω_0 units) computed for Ag using GGA-PBEsol functional and with spin-orbit coupling.

Ag	E^F	P_{11}	P_{22}	P_{33}	P_{12}	P_{23}	P_{31}	Ω_{11}	Ω_{22}	Ω_{33}	Ω_{12}	Ω_{23}	Ω_{31}	Ω^{rel}
$\langle 100 \rangle$ d	3.927	26.242	26.908	26.908	0.000	0.000	0.000	0.550	0.730	0.730	0.000	0.000	0.000	2.010
Octa	4.115	27.520	27.520	27.520	0.000	0.000	0.000	0.691	0.691	0.691	0.000	0.000	0.000	2.073
$\langle 110 \rangle$ c	4.134	26.579	26.579	28.915	12.833	0.000	0.000	0.477	0.477	1.107	1.216	0.000	0.000	2.061
$\langle 110 \rangle$ d	4.134	26.590	26.590	28.751	12.913	0.000	0.000	0.491	0.491	1.075	1.223	0.000	0.000	2.057
$\langle 111 \rangle$ d	4.498	27.924	27.924	27.924	4.043	4.043	4.043	0.701	0.701	0.701	0.382	0.382	0.382	2.104
Tetra	4.571	28.164	28.164	28.164	0.000	0.000	0.000	0.707	0.707	0.707	0.000	0.000	0.000	2.122
Vac	1.152	-4.244	-4.244	-4.244	0.000	0.000	0.000	-0.107	-0.107	-0.107	0.000	0.000	0.000	-0.320

TABLE XIX. Formation energy of a defect E^F (in eV units), elements of its dipole tensor P_{ij} (in eV units), and relaxation volume tensor Ω_{ij} (in Ω_0 units), as well as the relaxation volume of a defect Ω^{rel} (in Ω_0 units) computed for Ir using GGA-PBE functional.

Ir	E^F	P_{11}	P_{22}	P_{33}	P_{12}	P_{23}	P_{31}	Ω_{11}	Ω_{22}	Ω_{33}	Ω_{12}	Ω_{23}	Ω_{31}	Ω^{rel}
$\langle 100 \rangle$ d	8.687	58.928	67.113	67.113	0.000	0.000	0.000	0.484	0.726	0.726	0.000	0.000	0.000	1.935
Octa	8.754	65.520	65.520	65.520	0.000	0.000	0.000	0.656	0.656	0.656	0.000	0.000	0.000	1.969
$\langle 110 \rangle$ c	11.281	67.284	67.284	67.947	28.286	0.000	0.000	0.670	0.670	0.689	0.571	0.000	0.000	2.029
$\langle 110 \rangle$ d	11.280	67.514	67.514	67.459	28.406	0.000	0.000	0.677	0.677	0.675	0.573	0.000	0.000	2.029
$\langle 111 \rangle$ d	10.216	69.054	69.054	69.054	-2.850	-2.850	-2.850	0.692	0.692	0.692	-0.058	-0.058	-0.058	2.075
Tetra	10.075	68.144	68.144	68.144	0.000	0.000	0.000	0.683	0.683	0.683	0.000	0.000	0.000	2.048
Vac	1.519	-11.625	-11.625	-11.625	0.000	0.000	0.000	-0.116	-0.116	-0.116	0.000	0.000	0.000	-0.349

TABLE XX. Formation energy of a defect E^F (in eV units), elements of its dipole tensor P_{ij} (in eV units), and relaxation volume tensor Ω_{ij} (in Ω_0 units), as well as the relaxation volume of a defect Ω^{rel} (in Ω_0 units) computed for Ir using GGA-PBESol functional.

Ir	E^F	P_{11}	P_{22}	P_{33}	P_{12}	P_{23}	P_{31}	Ω_{11}	Ω_{22}	Ω_{33}	Ω_{12}	Ω_{23}	Ω_{31}	Ω^{rel}
$\langle 100 \rangle$ d	9.617	63.248	72.350	72.350	0.000	0.000	0.000	0.490	0.758	0.758	0.000	0.000	0.000	2.007
Octa	9.722	70.524	70.524	70.524	0.000	0.000	0.000	0.681	0.681	0.681	0.000	0.000	0.000	2.042
$\langle 110 \rangle$ c	12.330	71.954	71.954	73.819	30.345	0.000	0.000	0.682	0.682	0.737	0.602	0.000	0.000	2.101
$\langle 110 \rangle$ d	12.327	72.136	72.136	73.219	30.505	0.000	0.000	0.689	0.689	0.721	0.605	0.000	0.000	2.099
$\langle 111 \rangle$ d	11.303	74.124	74.124	74.124	-2.720	-2.720	-2.720	0.715	0.715	0.715	-0.054	-0.054	-0.054	2.146
Tetra	11.148	73.144	73.144	73.144	0.000	0.000	0.000	0.706	0.706	0.706	0.000	0.000	0.000	2.118
Vac	1.979	-13.024	-13.024	-13.024	0.000	0.000	0.000	-0.126	-0.126	-0.126	0.000	0.000	0.000	-0.377

TABLE XXI. Formation energy of a defect E^F (in eV units), elements of its dipole tensor P_{ij} (in eV units), and relaxation volume tensor Ω_{ij} (in Ω_0 units), as well as the relaxation volume of a defect Ω^{rel} (in Ω_0 units) computed for Ir using GGA-PBESol functional and with spin-orbit coupling.

Ir	E^F	P_{11}	P_{22}	P_{33}	P_{12}	P_{23}	P_{31}	Ω_{11}	Ω_{22}	Ω_{33}	Ω_{12}	Ω_{23}	Ω_{31}	Ω^{rel}
$\langle 100 \rangle$ d	9.232	61.638	71.707	71.708	0.000	0.000	0.000	0.473	0.774	0.774	0.000	0.000	0.000	2.021
Octa	9.294	69.418	69.418	69.418	0.000	0.000	0.000	0.684	0.684	0.684	0.000	0.000	0.000	2.053
$\langle 110 \rangle$ c	11.929	71.244	71.243	72.282	30.239	0.000	0.000	0.695	0.695	0.726	0.621	0.000	0.000	2.117
$\langle 110 \rangle$ d	11.928	71.470	71.470	71.847	30.404	0.000	0.000	0.702	0.702	0.713	0.624	0.000	0.000	2.117
$\langle 111 \rangle$ d	10.916	72.960	72.960	72.960	-2.378	-2.378	-2.378	0.719	0.719	0.719	-0.049	-0.049	-0.049	2.158
Tetra	10.809	72.096	72.096	72.096	0.000	0.000	0.000	0.711	0.711	0.711	0.000	0.000	0.000	2.132
Vac	1.779	-12.715	-12.715	-12.715	0.000	0.000	0.000	-0.125	-0.125	-0.125	0.000	0.000	0.000	-0.376

TABLE XXII. Formation energy of a defect E^F (in eV units), elements of its dipole tensor P_{ij} (in eV units), and relaxation volume tensor Ω_{ij} (in Ω_0 units), as well as the relaxation volume of a defect Ω^{rel} (in Ω_0 units) computed for Pt using GGA-PBE functional.

Pt	E^F	P_{11}	P_{22}	P_{33}	P_{12}	P_{23}	P_{31}	Ω_{11}	Ω_{22}	Ω_{33}	Ω_{12}	Ω_{23}	Ω_{31}	Ω^{rel}
$\langle 100 \rangle$ d	5.159	46.704	50.172	50.172	0.000	0.000	0.000	0.414	0.805	0.805	0.000	0.000	0.000	2.023
Octa	4.825	49.008	49.008	49.008	0.000	0.000	0.000	0.674	0.674	0.674	0.000	0.000	0.000	2.023
$\langle 110 \rangle$ c	5.699	51.100	51.100	50.519	16.330	0.000	0.000	0.722	0.722	0.657	1.406	0.000	0.000	2.101
$\langle 110 \rangle$ d	5.699	51.069	51.069	50.516	16.382	0.000	0.000	0.721	0.721	0.659	1.410	0.000	0.000	2.100
$\langle 111 \rangle$ d	5.634	50.876	50.876	50.876	0.870	0.870	0.870	0.700	0.700	0.700	0.075	0.075	0.075	2.100
Tetra	5.998	51.628	51.628	51.628	0.000	0.000	0.000	0.710	0.710	0.710	0.000	0.000	0.000	2.131
Vac	0.545	-11.054	-11.054	-11.054	0.000	0.000	0.000	-0.152	-0.152	-0.152	0.000	0.000	0.000	-0.456

TABLE XXIII. Formation energy of a defect E^F (in eV units), elements of its dipole tensor P_{ij} (in eV units), and relaxation volume tensor Ω_{ij} (in Ω_0 units), as well as the relaxation volume of a defect Ω^{rel} (in Ω_0 units) computed for Pt_pv using GGA-PBE functional.

Pt_pv	E^F	P_{11}	P_{22}	P_{33}	P_{12}	P_{23}	P_{31}	Ω_{11}	Ω_{22}	Ω_{33}	Ω_{12}	Ω_{23}	Ω_{31}	Ω^{rel}
$\langle 100 \rangle$ d	5.626	48.218	51.641	51.641	0.000	0.000	0.000	0.433	0.749	0.749	0.000	0.000	0.000	1.932
Octa	5.285	50.548	50.548	50.548	0.000	0.000	0.000	0.645	0.645	0.645	0.000	0.000	0.000	1.934
$\langle 110 \rangle$ c	6.182	52.523	52.523	52.129	17.058	0.000	0.000	0.680	0.680	0.644	1.267	0.000	0.000	2.004
$\langle 110 \rangle$ d	6.182	52.511	52.511	52.118	17.081	0.000	0.000	0.680	0.680	0.644	1.268	0.000	0.000	2.004
$\langle 111 \rangle$ d	6.122	52.466	52.466	52.466	0.999	0.999	0.999	0.669	0.669	0.669	0.074	0.074	0.074	2.007
Tetra	6.496	53.229	53.229	53.229	0.000	0.000	0.000	0.679	0.679	0.679	0.000	0.000	0.000	2.036
Vac	0.458	-11.177	-11.177	-11.177	0.000	0.000	0.000	-0.143	-0.143	-0.143	0.000	0.000	0.000	-0.428

TABLE XXIV. Formation energy of a defect E^F (in eV units), elements of its dipole tensor P_{ij} (in eV units), and relaxation volume tensor Ω_{ij} (in Ω_0 units), as well as the relaxation volume of a defect Ω^{rel} (in Ω_0 units) computed for Pt using GGA-PBEsol functional.

Pt	E^F	P_{11}	P_{22}	P_{33}	P_{12}	P_{23}	P_{31}	Ω_{11}	Ω_{22}	Ω_{33}	Ω_{12}	Ω_{23}	Ω_{31}	Ω^{rel}
$\langle 100 \rangle$ d	5.916	49.843	53.138	53.138	0.000	0.000	0.000	0.429	0.745	0.745	0.000	0.000	0.000	1.920
Octa	5.557	52.107	52.107	52.107	0.000	0.000	0.000	0.641	0.641	0.641	0.000	0.000	0.000	1.922
$\langle 110 \rangle$ c	6.528	54.035	54.035	54.015	18.748	0.000	0.000	0.665	0.665	0.663	1.307	0.000	0.000	1.993
$\langle 110 \rangle$ d	6.527	54.114	54.114	54.062	18.796	0.000	0.000	0.667	0.667	0.662	1.310	0.000	0.000	1.995
$\langle 111 \rangle$ d	6.484	54.130	54.130	54.130	1.047	1.047	1.047	0.666	0.666	0.666	0.073	0.073	0.073	1.997
Tetra	6.882	54.834	54.834	54.834	0.000	0.000	0.000	0.674	0.674	0.674	0.000	0.000	0.000	2.023
Vac	0.785	-14.305	-14.305	-14.305	0.000	0.000	0.000	-0.176	-0.176	-0.176	0.000	0.000	0.000	-0.528

TABLE XXV. Formation energy of a defect E^F (in eV units), elements of its dipole tensor P_{ij} (in eV units), and relaxation volume tensor Ω_{ij} (in Ω_0 units), as well as the relaxation volume of a defect Ω^{rel} (in Ω_0 units) computed for Pt using GGA-PBEsol functional and with spin-orbit coupling.

Pt	E^F	P_{11}	P_{22}	P_{33}	P_{12}	P_{23}	P_{31}	Ω_{11}	Ω_{22}	Ω_{33}	Ω_{12}	Ω_{23}	Ω_{31}	Ω^{rel}
$\langle 100 \rangle$ d	5.669	50.156	55.230	55.230	0.000	0.000	0.000	0.339	0.836	0.836	0.000	0.000	0.000	2.012
Octa	5.501	53.357	53.357	53.357	0.000	0.000	0.000	0.668	0.668	0.668	0.000	0.000	0.000	2.005
$\langle 110 \rangle$ c	6.243	55.108	55.107	55.829	17.222	0.000	0.000	0.670	0.670	0.740	1.139	0.000	0.000	2.080
$\langle 110 \rangle$ d	6.244	55.094	55.092	55.758	17.150	0.000	0.000	0.671	0.671	0.736	1.134	0.000	0.000	2.078
$\langle 111 \rangle$ d	6.317	55.341	55.341	55.341	0.823	0.823	0.823	0.693	0.693	0.693	0.054	0.054	0.054	2.079
Tetra	6.607	56.266	56.266	56.266	0.000	0.000	0.000	0.705	0.705	0.705	0.000	0.000	0.000	2.114
Vac	0.831	-11.837	-11.837	-11.837	0.000	0.000	0.000	-0.148	-0.148	-0.148	0.000	0.000	0.000	-0.445

TABLE XXVI. Formation energy of a defect E^F (in eV units), elements of its dipole tensor P_{ij} (in eV units), and relaxation volume tensor Ω_{ij} (in Ω_0 units), as well as the relaxation volume of a defect Ω^{rel} (in Ω_0 units) computed for Au using the GGA-PBE functional.

Au	E^F	P_{11}	P_{22}	P_{33}	P_{12}	P_{23}	P_{31}	Ω_{11}	Ω_{22}	Ω_{33}	Ω_{12}	Ω_{23}	Ω_{31}	Ω^{rel}
$\langle 100 \rangle$ d	2.738	30.818	32.140	32.140	0.000	0.000	0.000	-0.116	1.078	1.078	0.000	0.000	0.000	2.039
Octa	2.805	32.429	32.429	32.429	0.000	0.000	0.000	0.695	0.695	0.695	0.000	0.000	0.000	2.086
$\langle 110 \rangle$ c	2.602	32.627	32.627	31.825	9.558	0.000	0.000	0.935	0.935	0.212	1.941	0.000	0.000	2.081
$\langle 110 \rangle$ d	2.603	32.605	32.605	31.850	9.549	0.000	0.000	0.921	0.921	0.239	1.939	0.000	0.000	2.081
$\langle 111 \rangle$ d	3.195	33.669	33.669	33.669	2.521	2.521	2.521	0.722	0.722	0.722	0.512	0.512	0.512	2.166
Tetra	3.290	33.860	33.860	33.860	0.000	0.000	0.000	0.726	0.726	0.726	0.000	0.000	0.000	2.178
Vac	0.442	-5.379	-5.379	-5.379	0.000	0.000	0.000	-0.115	-0.115	-0.115	0.000	0.000	0.000	-0.346

TABLE XXVII. Formation energy of a defect E^F (in eV units), elements of its dipole tensor P_{ij} (in eV units), and relaxation volume tensor Ω_{ij} (in Ω_0 units), as well as the relaxation volume of a defect Ω^{rel} (in Ω_0 units) computed for Au_pv_GW using the GGA-PBE functional.

Au_pv_GW	E^F	P_{11}	P_{22}	P_{33}	P_{12}	P_{23}	P_{31}	Ω_{11}	Ω_{22}	Ω_{33}	Ω_{12}	Ω_{23}	Ω_{31}	Ω^{rel}
$\langle 100 \rangle$ d	2.787	31.037	32.345	32.345	0.000	0.000	0.000	0.179	0.894	0.894	0.000	0.000	0.000	1.968
Octa	2.853	32.651	32.651	32.651	0.000	0.000	0.000	0.671	0.671	0.671	0.000	0.000	0.000	2.013
$\langle 110 \rangle$ c	2.683	32.882	32.882	31.955	9.645	0.000	0.000	0.839	0.839	0.331	1.867	0.000	0.000	2.008
$\langle 110 \rangle$ d	2.683	32.882	32.882	31.958	9.648	0.000	0.000	0.838	0.838	0.332	1.867	0.000	0.000	2.009
$\langle 111 \rangle$ d	3.252	33.860	33.860	33.860	2.442	2.442	2.442	0.696	0.696	0.696	0.473	0.473	0.473	2.088
Tetra	3.336	34.051	34.051	34.051	0.000	0.000	0.000	0.700	0.700	0.700	0.000	0.000	0.000	2.100
Vac	0.418	-5.234	-5.234	-5.234	0.000	0.000	0.000	-0.108	-0.108	-0.108	0.000	0.000	0.000	-0.323

TABLE XXVIII. Formation energy of a defect E^F (in eV units), elements of its dipole tensor P_{ij} (in eV units), and relaxation volume tensor Ω_{ij} (in Ω_0 units), as well as the relaxation volume of a defect Ω^{rel} (in Ω_0 units) computed for Au using the GGA-PBESol functional.

Au	E^F	P_{11}	P_{22}	P_{33}	P_{12}	P_{23}	P_{31}	Ω_{11}	Ω_{22}	Ω_{33}	Ω_{12}	Ω_{23}	Ω_{31}	Ω^{rel}
$\langle 100 \rangle$ d	3.474	39.244	41.543	41.543	0.000	0.000	0.000	0.191	0.998	0.998	0.000	0.000	0.000	2.187
Octa	3.563	41.801	41.801	41.801	0.000	0.000	0.000	0.747	0.747	0.747	0.000	0.000	0.000	2.242
$\langle 110 \rangle$ c	3.375	41.381	41.381	40.870	12.244	0.000	0.000	0.797	0.797	0.617	1.757	0.000	0.000	2.210
$\langle 110 \rangle$ d	3.374	41.358	41.358	40.881	12.270	0.000	0.000	0.792	0.792	0.625	1.761	0.000	0.000	2.210
$\langle 111 \rangle$ d	4.031	42.621	42.621	42.621	3.605	3.605	3.605	0.762	0.762	0.762	0.517	0.517	0.517	2.286
Tetra	4.143	42.947	42.947	42.947	0.000	0.000	0.000	0.768	0.768	0.768	0.000	0.000	0.000	2.303
Vac	0.765	-5.289	-5.289	-5.289	0.000	0.000	0.000	-0.095	-0.095	-0.095	0.000	0.000	0.000	-0.284

TABLE XXIX. Formation energy of a defect E^F (in eV units), elements of its dipole tensor P_{ij} (in eV units), and relaxation volume tensor Ω_{ij} (in Ω_0 units), as well as the relaxation volume of a defect Ω^{rel} (in Ω_0 units) computed for Au using the GGA-PBESol functional with spin-orbit coupling.

Au	E^F	P_{11}	P_{22}	P_{33}	P_{12}	P_{23}	P_{31}	Ω_{11}	Ω_{22}	Ω_{33}	Ω_{12}	Ω_{23}	Ω_{31}	Ω^{rel}
$\langle 100 \rangle$ d	3.465	37.228	39.485	39.485	0.000	0.000	0.000	0.235	0.901	0.901	0.000	0.000	0.000	2.038
Octa	3.556	39.698	39.698	39.698	0.000	0.000	0.000	0.696	0.696	0.696	0.000	0.000	0.000	2.088
$\langle 110 \rangle$ c	3.370	39.261	39.261	38.899	12.435	0.000	0.000	0.722	0.722	0.615	1.638	0.000	0.000	2.059
$\langle 110 \rangle$ d	3.369	39.283	39.283	38.926	12.439	0.000	0.000	0.722	0.722	0.617	1.638	0.000	0.000	2.060
$\langle 111 \rangle$ d	4.041	40.563	40.563	40.563	3.733	3.733	3.733	0.711	0.711	0.711	0.491	0.491	0.491	2.134
Tetra	4.158	40.882	40.882	40.882	0.000	0.000	0.000	0.717	0.717	0.717	0.000	0.000	0.000	2.151
Vac	0.662	-8.199	-8.199	-8.199	0.000	0.000	0.000	-0.144	-0.144	-0.144	0.000	0.000	0.000	-0.431

TABLE XXX. Formation energy of a defect E^F (in eV units), elements of its dipole tensor P_{ij} (in eV units), and relaxation volume tensor Ω_{ij} (in Ω_0 units), as well as the relaxation volume of a defect Ω^{rel} (in Ω_0 units) computed for Au using the MetaGGA-RTPSS functional with spin-orbit coupling.

Au	E^F	P_{11}	P_{22}	P_{33}	P_{12}	P_{23}	P_{31}	Ω_{11}	Ω_{22}	Ω_{33}	Ω_{12}	Ω_{23}	Ω_{31}	Ω^{rel}
$\langle 100 \rangle$ d	3.938	36.667	39.612	39.612	0.000	0.000	0.000	0.231	0.888	0.888	0.000	0.000	0.000	2.008
Octa	4.102	39.529	39.529	39.529	0.000	0.000	0.000	0.685	0.685	0.685	0.000	0.000	0.000	2.055
$\langle 110 \rangle$ c	3.959	38.856	38.856	41.084	11.199	0.00000	0.000	0.520	0.520	1.018	1.062	0.000	0.000	2.058
$\langle 110 \rangle$ d	3.960	38.742	38.742	41.332	11.155	0.00000	0.000	0.494	0.494	1.072	1.057	0.000	0.000	2.059
$\langle 111 \rangle$ d	4.785	41.072	41.072	41.072	5.286	5.286	5.286	0.712	0.712	0.712	0.501	0.501	0.501	2.135
Tetra	4.879	41.277	41.277	41.277	0.000	0.000	0.000	0.715	0.715	0.715	0.000	0.000	0.000	2.146
Vac	0.939	-6.760	-6.760	-6.760	0.000	0.000	0.000	-0.117	-0.117	-0.117	0.000	0.000	0.000	-0.351

TABLE XXXI. Formation energy of a defect E^F (in eV units), elements of its dipole tensor P_{ij} (in eV units), and relaxation volume tensor Ω_{ij} (in Ω_0 units), as well as the relaxation volume of a defect Ω^{rel} (in Ω_0 units) computed for Pb using the GGA-PBE functional.

Pb	E^F	P_{11}	P_{22}	P_{33}	P_{12}	P_{23}	P_{31}	Ω_{11}	Ω_{22}	Ω_{33}	Ω_{12}	Ω_{23}	Ω_{31}	Ω^{rel}
$\langle 100 \rangle$ d	1.264	12.361	12.912	12.912	0.000	0.000	0.000	0.393	0.589	0.589	0.000	0.000	0.000	1.570
Octa	1.254	13.466	13.466	13.466	0.000	0.000	0.000	0.554	0.554	0.554	0.000	0.000	0.000	1.661
$\langle 110 \rangle$ c	1.366	11.890	11.890	13.262	5.231	0.000	0.000	0.345	0.345	0.833	0.662	0.000	0.000	1.523
$\langle 110 \rangle$ d	1.367	11.831	11.831	13.243	5.236	0.000	0.000	0.338	0.338	0.841	0.663	0.000	0.000	1.517
$\langle 111 \rangle$ d	1.418	12.364	12.364	12.364	0.777	0.777	0.777	0.508	0.508	0.508	0.098	0.098	0.098	1.525
Tetra	1.428	12.405	12.405	12.405	0.000	0.000	0.000	0.510	0.510	0.510	0.000	0.000	0.000	1.530
Vac	0.299	-2.769	-2.769	-2.769	0.000	0.000	0.000	-0.114	-0.114	-0.114	0.000	0.000	0.000	-0.342

TABLE XXXII. Formation energy of a defect E^F (in eV units), elements of its dipole tensor P_{ij} (in eV units), and relaxation volume tensor Ω_{ij} (in Ω_0 units), as well as the relaxation volume of a defect Ω^{rel} (in Ω_0 units) computed for Pb_d using the GGA-PBE functional.

Pb_d	E^F	P_{11}	P_{22}	P_{33}	P_{12}	P_{23}	P_{31}	Ω_{11}	Ω_{22}	Ω_{33}	Ω_{12}	Ω_{23}	Ω_{31}	Ω^{rel}
$\langle 100 \rangle$ d	1.307	12.796	13.222	13.222	0.000	0.000	0.000	0.436	0.555	0.555	0.000	0.000	0.000	1.546
Octa	1.295	13.732	13.732	13.732	0.000	0.000	0.000	0.541	0.541	0.541	0.000	0.000	0.000	1.623
$\langle 110 \rangle$ c	1.418	11.941	11.941	13.452	5.240	0.000	0.000	0.349	0.349	0.772	0.604	0.000	0.000	1.471
$\langle 110 \rangle$ d	1.418	12.170	12.170	13.641	5.222	0.000	0.000	0.361	0.361	0.774	0.602	0.000	0.000	1.496
$\langle 111 \rangle$ d	1.469	12.877	12.877	12.877	0.799	0.799	0.799	0.507	0.507	0.507	0.092	0.092	0.092	1.522
Tetra	1.478	12.846	12.846	12.846	0.000	0.000	0.000	0.506	0.506	0.506	0.000	0.000	0.000	1.518
Vac	0.285	-2.342	-2.342	-2.342	0.000	0.000	0.000	-0.092	-0.092	-0.092	0.000	0.000	0.000	-0.277

TABLE XXXIII. Formation energy of a defect E^F (in eV units), elements of its dipole tensor P_{ij} (in eV units), and relaxation volume tensor Ω_{ij} (in Ω_0 units), as well as the relaxation volume of a defect Ω^{rel} (in Ω_0 units) computed for Pb_d_GW using the GGA-PBE functional.

Pb_d_GW	E^F	P_{11}	P_{22}	P_{33}	P_{12}	P_{23}	P_{31}	Ω_{11}	Ω_{22}	Ω_{33}	Ω_{12}	Ω_{23}	Ω_{31}	Ω^{rel}
$\langle 100 \rangle$ d	1.297	12.519	12.909	12.909	0.000	0.000	0.000	0.442	0.578	0.578	0.000	0.000	0.000	1.597
Octa	1.285	13.413	13.413	13.413	0.000	0.000	0.000	0.559	0.559	0.559	0.000	0.000	0.000	1.676
$\langle 110 \rangle$ c	1.407	11.974	11.974	13.386	5.186	0.000	0.000	0.355	0.355	0.846	0.621	0.000	0.000	1.555
$\langle 110 \rangle$ d	1.407	11.976	11.976	13.387	5.181	0.000	0.000	0.355	0.355	0.846	0.620	0.000	0.000	1.555
$\langle 111 \rangle$ d	1.460	12.489	12.489	12.489	0.765	0.765	0.765	0.520	0.520	0.520	0.092	0.092	0.092	1.561
Tetra	1.470	12.513	12.513	12.513	0.000	0.000	0.000	0.521	0.521	0.521	0.000	0.000	0.000	1.564
Vac	0.279	-2.660	-2.660	-2.660	0.000	0.000	0.000	-0.111	-0.111	-0.111	0.000	0.000	0.000	-0.332

TABLE XXXIV. Formation energy of a defect E^F (in eV units), elements of its dipole tensor P_{ij} (in eV units), and relaxation volume tensor Ω_{ij} (in Ω_0 units), as well as the relaxation volume of a defect Ω^{rel} (in Ω_0 units) computed for Pb using the GGA-PBESol functional.

Pb	E^F	P_{11}	P_{22}	P_{33}	P_{12}	P_{23}	P_{31}	Ω_{11}	Ω_{22}	Ω_{33}	Ω_{12}	Ω_{23}	Ω_{31}	Ω^{rel}
$\langle 100 \rangle$ d	1.365	13.638	14.419	14.419	0.000	0.000	0.000	0.246	0.693	0.693	0.000	0.000	0.000	1.631
Octa	1.377	14.900	14.900	14.900	0.000	0.000	0.000	0.572	0.572	0.572	0.000	0.000	0.000	1.716
$\langle 110 \rangle$ c	1.420	12.999	12.999	14.723	5.901	0.000	0.000	0.193	0.193	1.178	1.139	0.000	0.000	1.564
$\langle 110 \rangle$ d	1.421	13.033	13.033	14.707	5.883	0.000	0.000	0.203	0.203	1.159	1.136	0.000	0.000	1.566
$\langle 111 \rangle$ d	1.493	13.768	13.768	13.768	0.897	0.897	0.897	0.529	0.529	0.529	0.173	0.173	0.173	1.586
Tetra	1.501	13.728	13.728	13.728	0.009	0.009	0.009	0.527	0.527	0.527	0.000	0.000	0.000	1.581
Vac	0.407	-3.235	-3.235	-3.235	0.000	0.000	0.000	-0.124	-0.124	-0.124	0.000	0.000	0.000	-0.373

TABLE XXXV. Formation energy of a defect E^F (in eV units), elements of its dipole tensor P_{ij} (in eV units), and relaxation volume tensor Ω_{ij} (in Ω_0 units), as well as the relaxation volume of a defect Ω^{rel} (in Ω_0 units) computed for Pb using the GGA-PBESol functional with spin-orbit coupling.

Pb	E^F	P_{11}	P_{22}	P_{33}	P_{12}	P_{23}	P_{31}	Ω_{11}	Ω_{22}	Ω_{33}	Ω_{12}	Ω_{23}	Ω_{31}	Ω^{rel}
$\langle 100 \rangle$ d	1.001	12.897	13.436	13.436	0.000	0.000	0.000	0.411	0.559	0.559	0.000	0.000	0.000	1.528
Octa	0.987	13.863	13.863	13.863	0.000	0.000	0.000	0.533	0.533	0.533	0.000	0.000	0.000	1.598
$\langle 110 \rangle$ c	1.091	12.735	12.736	12.776	3.646	0.000	0.000	0.486	0.486	0.497	0.397	0.000	0.000	1.470
$\langle 110 \rangle$ d	1.092	12.769	12.769	12.754	3.693	0.000	0.000	0.492	0.492	0.488	0.402	0.000	0.000	1.471
$\langle 111 \rangle$ d	1.148	12.810	12.810	12.810	0.629	0.629	0.629	0.492	0.492	0.492	0.068	0.068	0.068	1.477
Tetra	1.155	12.867	12.867	12.867	0.000	0.000	0.000	0.494	0.494	0.494	0.000	0.000	0.000	1.483
Vac	0.295	-3.543	-3.543	-3.543	0.000	0.000	0.000	-0.136	-0.136	-0.136	0.000	0.000	0.000	-0.408

TABLE XXXVI. Formation energy of a defect E^F (in eV units), elements of its dipole tensor P_{ij} (in eV units), and relaxation volume tensor Ω_{ij} (in Ω_0 units), as well as the relaxation volume of a defect Ω^{rel} (in Ω_0 units) computed for Th using the GGA-PBE functional.

Th	E^F	P_{11}	P_{22}	P_{33}	P_{12}	P_{23}	P_{31}	Ω_{11}	Ω_{22}	Ω_{33}	Ω_{12}	Ω_{23}	Ω_{31}	Ω^{rel}
$\langle 100 \rangle$ d	4.968	23.098	21.820	21.820	0.000	0.000	0.000	0.757	0.621	0.621	0.000	0.000	0.000	1.998
Octa	4.802	21.500	21.500	21.500	0.000	0.000	0.000	0.644	0.644	0.644	0.000	0.000	0.000	1.931
$\langle 110 \rangle$ c	5.628	22.549	22.549	26.432	16.818	0.000	0.000	0.575	0.575	0.991	0.729	0.000	0.000	2.142
$\langle 110 \rangle$ d	5.623	22.544	22.544	26.321	16.789	0.000	0.000	0.578	0.578	0.982	0.728	0.000	0.000	2.138
$\langle 111 \rangle$ d	5.249	23.119	23.119	23.119	4.641	4.641	4.641	0.692	0.692	0.692	0.201	0.201	0.201	2.077
Tetra	5.344	22.576	22.576	22.576	0.000	0.000	0.000	0.676	0.676	0.676	0.000	0.000	0.000	2.028
Vac	2.444	-3.681	-3.681	-3.681	0.000	0.000	0.000	-0.110	-0.110	-0.110	0.000	0.000	0.000	-0.331

TABLE XXXVII. Formation energy of a defect E^F (in eV units), elements of its dipole tensor P_{ij} (in eV units), and relaxation volume tensor Ω_{ij} (in Ω_0 units), as well as the relaxation volume of a defect Ω^{rel} (in Ω_0 units) computed for Th using the GGA-PBESol functional.

Th	E^F	P_{11}	P_{22}	P_{33}	P_{12}	P_{23}	P_{31}	Ω_{11}	Ω_{22}	Ω_{33}	Ω_{12}	Ω_{23}	Ω_{31}	Ω^{rel}
$\langle 100 \rangle$ d	5.461	24.051	22.497	22.497	0.000	0.000	0.000	0.791	0.605	0.605	0.000	0.000	0.000	2.002
Octa	5.270	22.008	22.008	22.008	0.000	0.000	0.000	0.638	0.638	0.638	0.000	0.000	0.000	1.914
$\langle 110 \rangle$ c	6.211	23.759	23.759	27.005	18.480	0.000	0.000	0.591	0.591	0.979	0.764	0.000	0.000	2.161
$\langle 110 \rangle$ d	6.201	23.748	23.748	26.937	18.729	0.000	0.000	0.592	0.592	0.974	0.775	0.000	0.000	2.158
$\langle 111 \rangle$ d	5.792	23.897	23.897	23.897	5.184	5.184	5.184	0.693	0.693	0.693	0.214	0.214	0.214	2.079
Tetra	5.863	23.285	23.285	23.285	0.000	0.000	0.000	0.675	0.675	0.675	0.000	0.000	0.000	2.025
Vac	2.668	-4.741	-4.741	-4.741	0.000	0.000	0.000	-0.137	-0.137	-0.137	0.000	0.000	0.000	-0.412

TABLE XXXVIII. Formation energy of a defect E^F (in eV units), elements of its dipole tensor P_{ij} (in eV units), and relaxation volume tensor Ω_{ij} (in Ω_0 units), as well as the relaxation volume of a defect Ω^{rel} (in Ω_0 units) computed for Th using the GGA-PBESol functional with spin-orbit coupling.

Th	E^F	P_{11}	P_{22}	P_{33}	P_{12}	P_{23}	P_{31}	Ω_{11}	Ω_{22}	Ω_{33}	Ω_{12}	Ω_{23}	Ω_{31}	Ω^{rel}
$\langle 100 \rangle$ d	5.376	24.381	21.668	21.668	0.000	0.000	0.000	0.839	0.530	0.530	0.000	0.000	0.000	1.899
Octa	5.159	20.765	20.765	20.765	0.000	0.000	0.000	0.582	0.582	0.582	0.000	0.000	0.000	1.747
$\langle 110 \rangle$ c	6.179	23.778	23.778	24.927	19.466	0.000	0.000	0.634	0.634	0.765	0.815	0.000	0.000	2.032
$\langle 110 \rangle$ d	6.171	23.806	23.806	24.919	19.657	0.000	0.000	0.636	0.636	0.763	0.822	0.000	0.000	2.034
$\langle 111 \rangle$ d	5.745	23.192	23.192	23.192	5.739	5.739	5.739	0.650	0.650	0.650	0.240	0.240	0.240	1.951
Tetra	5.821	22.293	22.293	22.293	0.000	0.000	0.000	0.625	0.625	0.625	0.000	0.000	0.000	1.875
Vac	2.458	-4.609	-4.609	-4.609	0.000	0.000	0.000	-0.129	-0.129	-0.129	0.000	0.000	0.000	-0.388

TABLE XXXIX. Vacancy formation energy in Pb calculated using various cell size and k -point mesh.

Size	k points	E_{el}^{corr}	E_V^F
$2 \times 2 \times 2$	$6 \times 6 \times 6$	0.0125	0.507
$2 \times 2 \times 2$	$11 \times 11 \times 11$	0.0151	0.464
$3 \times 3 \times 3$	$4 \times 4 \times 4$	0.0028	0.443
$4 \times 4 \times 4$	$3 \times 3 \times 3$	0.0013	0.300
$4 \times 4 \times 4$	$4 \times 4 \times 4$	0.0031	0.407
$5 \times 5 \times 5$	$3 \times 3 \times 3$	0.0008	0.474

Calculations performed using the PBE functional tend to underestimate E_V^F . This was recognized to result from the underestimation of the exchange energy at the surface of a vacancy, whereas the correlation energy is overestimated only slightly [95]. The largest discrepancy with other DFT calculations is found for Pt and Pb. We performed comprehensive calculations using various supercell sizes and k -point meshes. They are listed in Tables XXXIX and XL. The supercell size effect is clearly significant. Our results are compatible other DFT studies where the same supercell size and k -point mesh were used. Medasani *et al.* [93] and Nazarov *et al.* [57] used small supercells containing $2 \times 2 \times 2$ unit cells. Angsten *et al.* [59] used larger supercells containing $3 \times 3 \times 3$ unit cells.

We also performed calculations using the PBEsol functional, which was developed to provide a better description of jellium surfaces [82]. We observe that the calculated values of E_V^F show better agreement with experimental data and are compatible with DFT calculations by Medasani *et al.* [93]. For some selected elements, including Cu, Ag, Ir, Pt, Au, Pb, and Th, we also performed calculations using PBEsol and including spin-orbit coupling. However, the resulting formation energies are not significantly different from those computed without spin-orbit coupling. A possible reason is that all the above metals are nonmagnetic, even though some of them are heavy elements characterized by relatively large values of the spin-orbit coupling parameter.

Since vacancy is elastically isotropic, its elastic dipole tensor P_{ij} is diagonal, and all the diagonal elements are the same, $P_{11} = P_{22} = P_{33}$. We have also calculated the relaxation volume Ω^{rel} of a vacancy from its dipole tensor P_{ij} . The relaxation volume of a defect is defined as the change of the total volume of a sample resulting from the relaxation of the lattice around a defect [96]. For a vacancy, the relaxation volume is negative. The experimentally observed values of vacancy relaxation volumes [97] are summarized in Table XLI. The

TABLE XL. Vacancy formation energy in Pt calculated using various cell size and k -point mesh.

Size	k points	E_{el}^{corr}	E_V^F
$2 \times 2 \times 2$	$6 \times 6 \times 6$	0.0514	0.735
$2 \times 2 \times 2$	$11 \times 11 \times 11$	0.0507	0.711
$3 \times 3 \times 3$	$4 \times 4 \times 4$	0.0162	0.624
$4 \times 4 \times 4$	$3 \times 3 \times 3$	0.0071	0.545
$4 \times 4 \times 4$	$4 \times 4 \times 4$	0.0085	0.600
$5 \times 5 \times 5$	$3 \times 3 \times 3$	0.0077	0.639

TABLE XLI. Experimentally observed vacancy and SIA relaxation volumes taken from Ref. [97].

Element	Ω_{SIA}^{rel}	Ω_V^{rel}
Al	1.9	-0.05/-0.38
Ni	1.8	-0.2
Cu	1.55 ± 0.2	-0.25
Pt	1.6 to 1.8	-0.28 to -0.42
Au	-	-0.15/-0.44

calculated relaxation volumes are generally compatible with the experimental values, taking into account the fact that there are large fluctuations of the experimentally observed values themselves.

In Fig. 2, we plotted vacancy relaxation volumes computed for metals where calculations were performed using the PBE and PBEsol functionals with and without spin-orbit coupling. We find no clear trend associated either with the use of a specific exchange-correlation functional, or with the effect of spin-orbit coupling. Calculations predict broadly similar relaxation volumes, although in some cases the computed values differ by as much as 25%.

B. Self-interstitial atom defects

The central result of this study is a comprehensive compilation of formation energies and anisotropic elastic parameters of SIA defects in FCC metals. We have plotted the formation energies of SIA configurations in various FCC metals, relative to the formation energy of a $\langle 100 \rangle$ dumbbell, in Figs. 3 to 12. The order in which SIA configurations are shown on the horizontal axis follows the sequence of formation energies found in Al.

We see that the most stable SIA configuration in Al, Ca, Ni, Cu, Pd, and Ag is a $\langle 100 \rangle$ dumbbell. However, the $\langle 100 \rangle$ SIA dumbbell does not represent the universally most stable defect structure in all the FCC metals. The octahedral site interstitial configuration, where an extra atom occupies the center of a cubic unit cell, is energetically more stable in Pt, Rh, and Th.

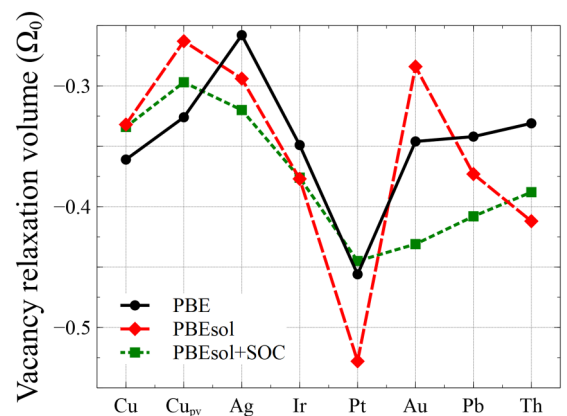


FIG. 2. Relaxation volumes of vacancies, expressed in atomic volume units Ω_0 , in Cu, Cu_{pv}, Ag, Ir, Pt, Au, Pb, and Th, calculated using exchange-correlation PBE and PBEsol functionals with and without spin-orbit coupling (SOC).

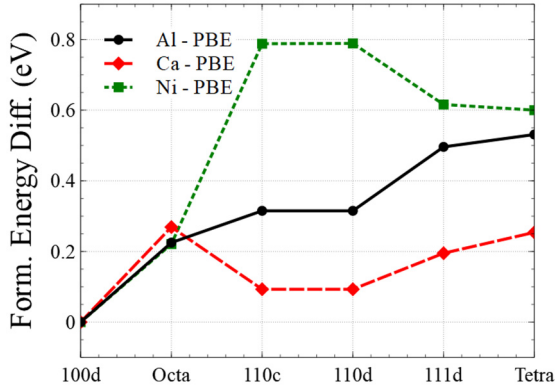


FIG. 3. Formation energies of various self-interstitial atom (SIA) defect configurations in Al, Ca, and Ni. In each case, the energy of a $\langle 100 \rangle$ dumbbell is used as a reference, and the curves show the difference between the energy of a given defect configuration and that of a $\langle 100 \rangle$ dumbbell.

Furthermore, it appears that the answer to the question about the stability of defects is not immediately straightforward for Sr, Ir, Au, and Pb.

In strontium (Sr), the formation energy of either a $\langle 110 \rangle$ crowdion or a dumbbell is higher than that of a $\langle 100 \rangle$ dumbbell, but the difference is just 0.016 eV. In iridium (Ir), the formation energy of an octahedral self-interstitial defect is 0.067 eV higher than that of a $\langle 100 \rangle$ dumbbell. In both metals, the $\langle 100 \rangle$ dumbbell configuration has the lowest energy, but the difference between the lowest and the second lowest formation energies is very small.

For gold (Au), the calculations performed using PBE, PBEsol, and PBEsol functionals with spin-orbit coupling suggest that a $\langle 110 \rangle$ crowdion or a $\langle 110 \rangle$ dumbbell are more stable than a $\langle 100 \rangle$ dumbbell. On the other hand, if the rTPSS functional with spin-orbit coupling is used, we find that the $\langle 100 \rangle$ dumbbell is the most stable configuration. Still, its formation energy is just 0.021 eV lower than the formation energy of a $\langle 110 \rangle$ crowdion.

For lead (Pb), calculations using the PBE functional, with various PAW potentials, and the PBEsol functional with spin-

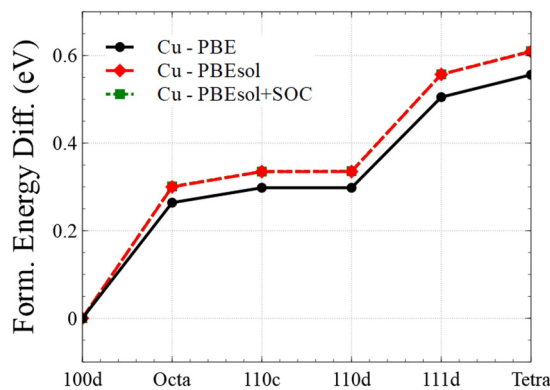


FIG. 4. Formation energies of various self-interstitial atom (SIA) defect configurations in Cu. The energy of a $\langle 100 \rangle$ dumbbell is used as a reference, and the curves show the difference between the energy of a given defect configuration and that of a $\langle 100 \rangle$ dumbbell.

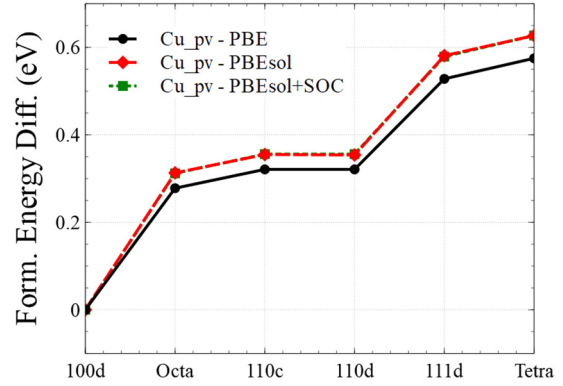


FIG. 5. Formation energies of various self-interstitial atom (SIA) defect configurations in Cu_{pV}. The energy of a $\langle 100 \rangle$ dumbbell is used as a reference, and the curves show the difference between the energy of a given defect configuration and that of a $\langle 100 \rangle$ dumbbell.

orbit coupling suggest that the octahedral site interstitial structure represents the most stable configuration of the defect. On the other hand, calculations performed using PBEsol suggest a $\langle 100 \rangle$ dumbbell ground state configuration instead. This conclusion is confirmed by calculations performed using a variety of starting atomic configurations. Using both functionals, we find that the difference between the energies of competing configurations is in the range from 0.010 to 0.012 eV. Given this tiny energy difference, it is difficult to ascertain what defect configuration is more stable in Pb.

A review of published literature results shows a small number of DFT studies of SIA defects in Al and Ni, and no studies of such defects in other FCC metals. Jesson *et al.* [67] performed orbital-free DFT investigation of Al. The general trend exhibited by the formation energies of defect configurations is similar to that found in our simulations, but their energy values are about 1 eV smaller than our results for all the SIA defects. The more recent work by Qui *et al.* [66] included both orbital-free and Kohn-Sham DFT studies of Al. These results are compatible with our calculations. Simulations of defects in Al were also performed using diffusion quantum Monte

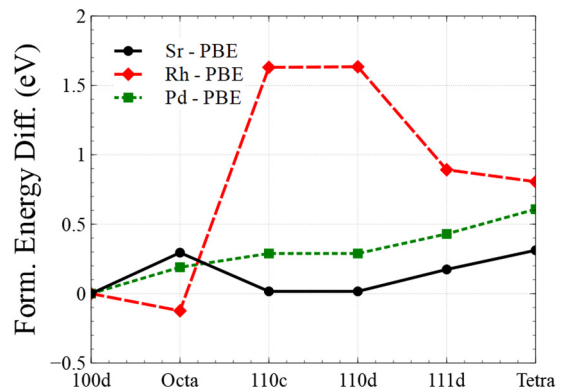


FIG. 6. Formation energies of various self-interstitial atom (SIA) defect configurations in Sr, Rh, and Pd. The energy of a $\langle 100 \rangle$ dumbbell is used as a reference, and the curves show the difference between the energy of a given defect configuration and that of a $\langle 100 \rangle$ dumbbell.

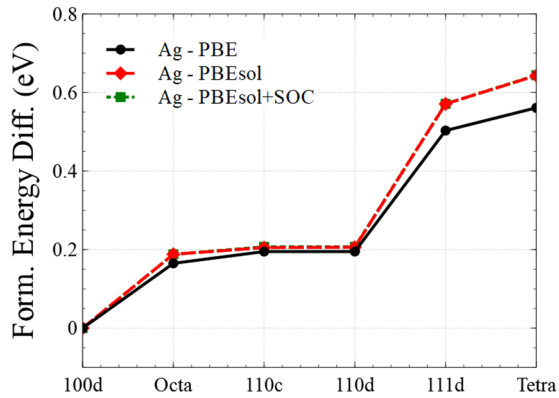


FIG. 7. Formation energies of various self-interstitial atom (SIA) defect configurations in Ag. The energy of a $\langle 100 \rangle$ dumbbell is used as a reference, and the curves show the difference between the energy of a given defect configuration and that of a $\langle 100 \rangle$ dumbbell.

Carlo (DMC), see Ref. [69]. They only investigated a $\langle 100 \rangle$ dumbbell, tetrahedral and octahedral site self-interstitials. The formation energies found in [69] are similar to those found in our DFT calculations. Tucker *et al.* [68] performed DFT simulations of SIA defects in Ni using VASP and found E_{SIA}^F values similar to those given below.

Our DFT results extend the currently limited data on SIA configurations in FCC metals. We show that the commonly used assumption that the $\langle 100 \rangle$ dumbbell configurations represent the most stable SIA defect structures does not uniformly apply to all the FCC metals, although our DFT results do confirm that a $\langle 100 \rangle$ dumbbell represents the ground state of the defect in Al, Ni and Cu in agreement with experimental observations [71–73].

Figures 13 to 16 show two-dimensional plots of electron charge density difference in Al, Cu, and Pb computed using the PBE functional. The defect structures in copper shown in the figures were investigated using the Cu_pv PAW potential. In the treatment of electronic structure of copper, the $3p$ orbitals were included as semicore valence states, and the corresponding results for copper in the VASP terminology are referred to as those for Cu_pv.

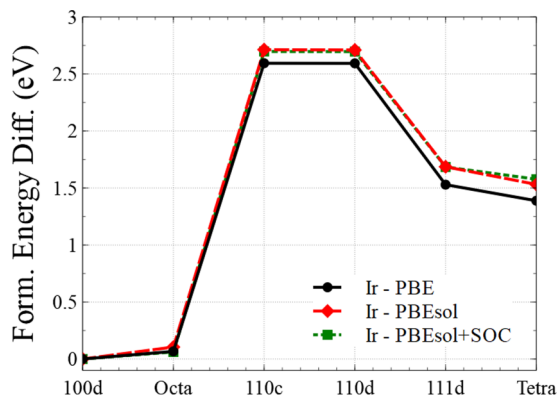


FIG. 8. Formation energies of various self-interstitial atom (SIA) defect configurations in Ir. The energy of a $\langle 100 \rangle$ dumbbell is used as a reference, and the curves show the difference between the energy of a given defect configuration and that of a $\langle 100 \rangle$ dumbbell.

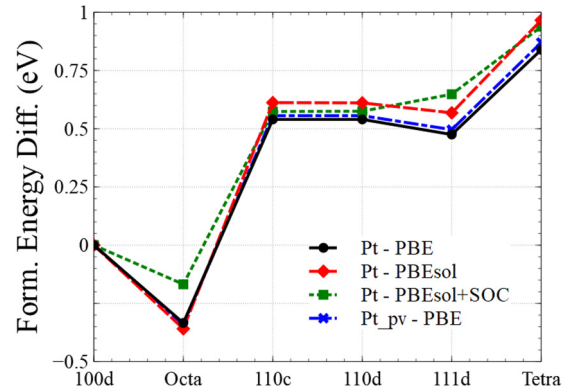


FIG. 9. Formation energies of various self-interstitial atom (SIA) defect configurations in Pt. The energy of a $\langle 100 \rangle$ dumbbell is used as a reference, and the curves show the difference between the energy of a given defect configuration and that of a $\langle 100 \rangle$ dumbbell.

The charge density difference plots shown in the figures were evaluated for the $\langle 100 \rangle$ dumbbell and octahedral site self-interstitials in the (010) and (011) planes. Electron charge density difference is defined as the fully convergent electron density computed *ab initio* minus the superposition of atomic charge densities. The plots illustrate different character of interatomic bonding in Al, Cu, and Pb. Bonding between atoms in Al and Pb is mainly mediated by s and p valence electrons, whereas bonding in Cu is mediated almost exclusively by s electrons. We observe the directional bonds forming around the core of the defect in Al and Pb. In Cu, on the other hand, the electron charge density remains largely nondirectional. We note that while being remarkable in its own right, this electronic structure phenomenon does not explain why a $\langle 100 \rangle$ dumbbell is stable in Al and Cu, and octahedral site self-interstitial is stable in Pb.

The character of the most stable SIA configuration determines the migration pathway and the type of thermal migration exhibited by the defect. Understanding the diffusion of SIA defects requires examining the migration pathway of an SIA defect in each metal.

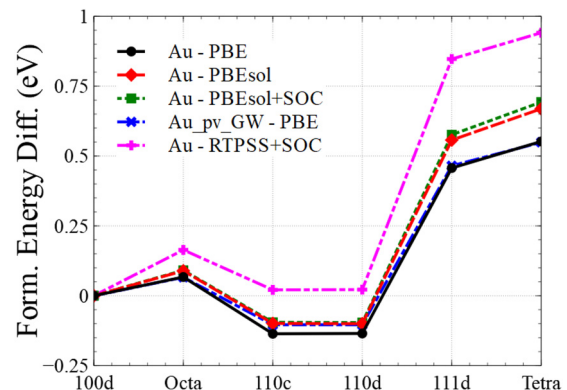


FIG. 10. Formation energies of various self-interstitial atom (SIA) defect configurations in Au. The energy of a $\langle 100 \rangle$ dumbbell is used as a reference, and the curves show the difference between the energy of a given defect configuration and that of a $\langle 100 \rangle$ dumbbell.

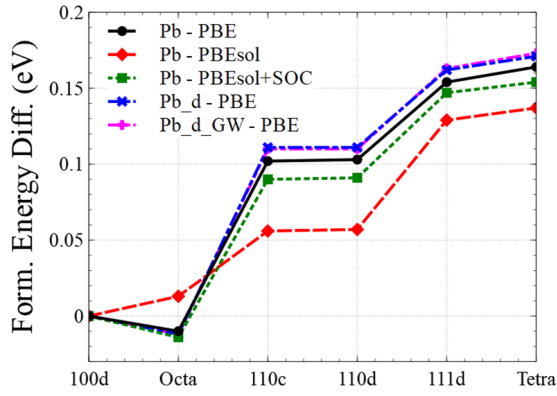


FIG. 11. Formation energies of various self-interstitial atom (SIA) defect configurations in Pb. The energy of a $\langle 100 \rangle$ dumbbell is used as a reference, and the curves show the difference between the energy of a given defect configuration and that of a $\langle 100 \rangle$ dumbbell.

Temperature T_{ID} , corresponding to stage I_D of recovery in electron irradiated resistivity recovery experiments, characterizes the onset of migration of SIA defects. Experimentally observed values of T_{ID} and SIA migration enthalpy H_I^M from Ref. [97] are summarized in Table XLII.

A $[100]$ dumbbell in an FCC metal migrates following a translation-rotation pathway to one of the $[010]$ or $[001]$ dumbbell configurations centered on one of the adjacent lattice sites [71–73,98]. In total, there are 8 pathways equivalent by symmetry. A schematic illustration showing one of the pathways is given in Fig. 17. Jesson *et al.* [67] performed orbital-free DFT calculations suggesting that the migration barrier is 0.084 eV in Al. Qui *et al.* performed orbital-free DFT calculations, involving various approximations, and found that the migration barrier was close to 0.11 eV. Tucker *et al.* calculated the SIA migration barrier in Ni using VASP and found that the value was close to 0.14 eV.

If we assume that the lowest energy state of a self-interstitial defect is octahedral, its nearest transition configuration is a $\langle 100 \rangle$ dumbbell. Therefore the comparatively low T_{ID} of Pb likely imply one-dimensional diffusion involving Octa \rightarrow $\langle 100 \rangle \rightarrow$ Octa transition pathways. A schematic illus-

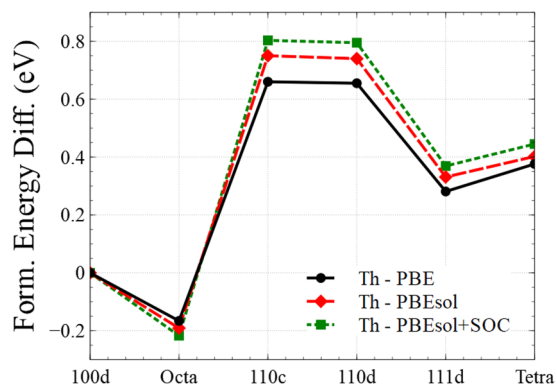


FIG. 12. Formation energies of various self-interstitial atom (SIA) defect configurations in Th. The energy of a $\langle 100 \rangle$ dumbbell is used as a reference, and the curves show the difference between the energy of a given defect configuration and that of a $\langle 100 \rangle$ dumbbell.

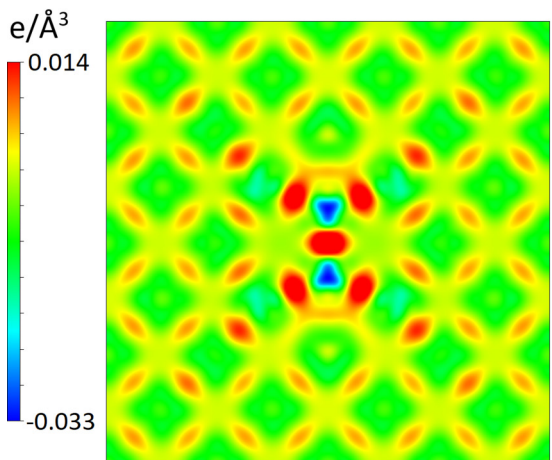
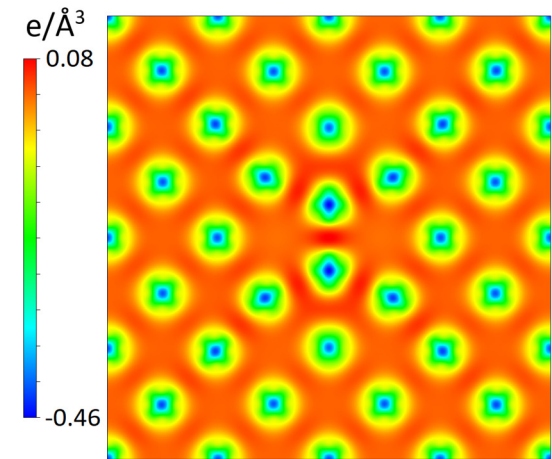
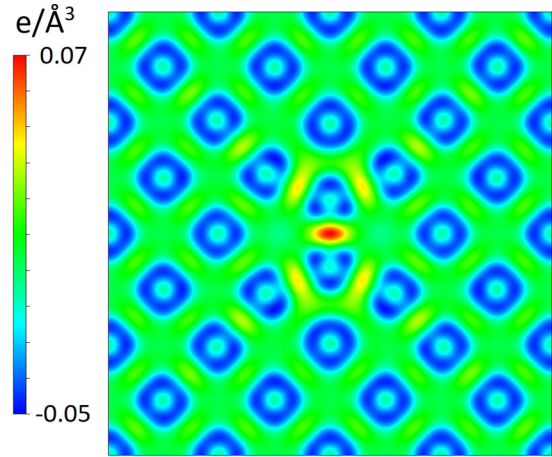


FIG. 13. Two-dimensional plots of the electron charge density difference in Al (top), Cu (middle), and Pb (bottom), computed for a $\langle 100 \rangle$ dumbbell configuration in a $\{010\}$ plane. Electron charge density difference is defined as the fully convergent electron density derived from *ab initio* simulations minus the superposition of atomic charge densities.

tration of such a pathway is given in Fig. 18. The migration enthalpy for this process is $H_I^M = 0.01$ eV, and this is compatible with the energy difference between the two lowest-energy SIA configurations. On the other hand, even though Rh and Th adopt an octahedral site interstitial configuration, their T_{ID} are

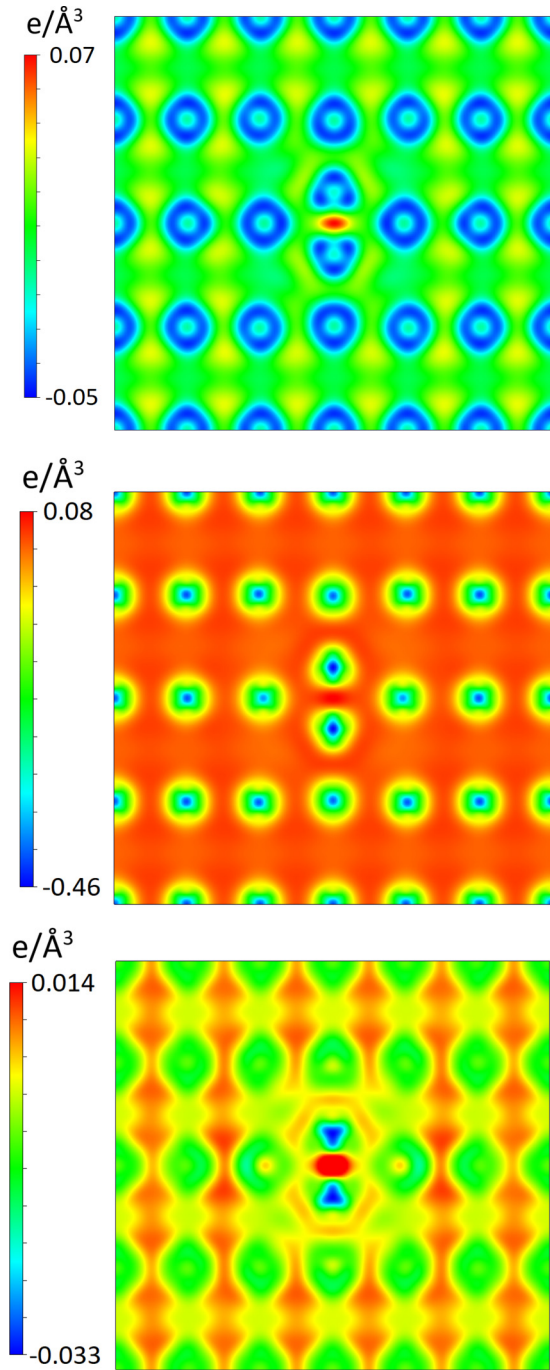


FIG. 14. Two-dimensional plots of the electron charge density difference in Al (top), Cu (middle), and Pb (bottom), computed for a $\langle 100 \rangle$ dumbbell configuration in a $\{011\}$ plane.

not very low, which is correlated with the fact that the energy difference between the two lowest energy SIA configurations is close to 0.1 eV.

The most surprising experimentally observed value of T_{ID} is the one for Au. A possible explanation is that a SIA in Au adopts a $\langle 110 \rangle$ crowdion/dumbbell configuration, and migrates purely one dimensionally following a sequence of crowdion \rightarrow dumbbell \rightarrow crowdion transformations, similarly to the migration of a $\langle 111 \rangle$ defects in BCC metals [99].

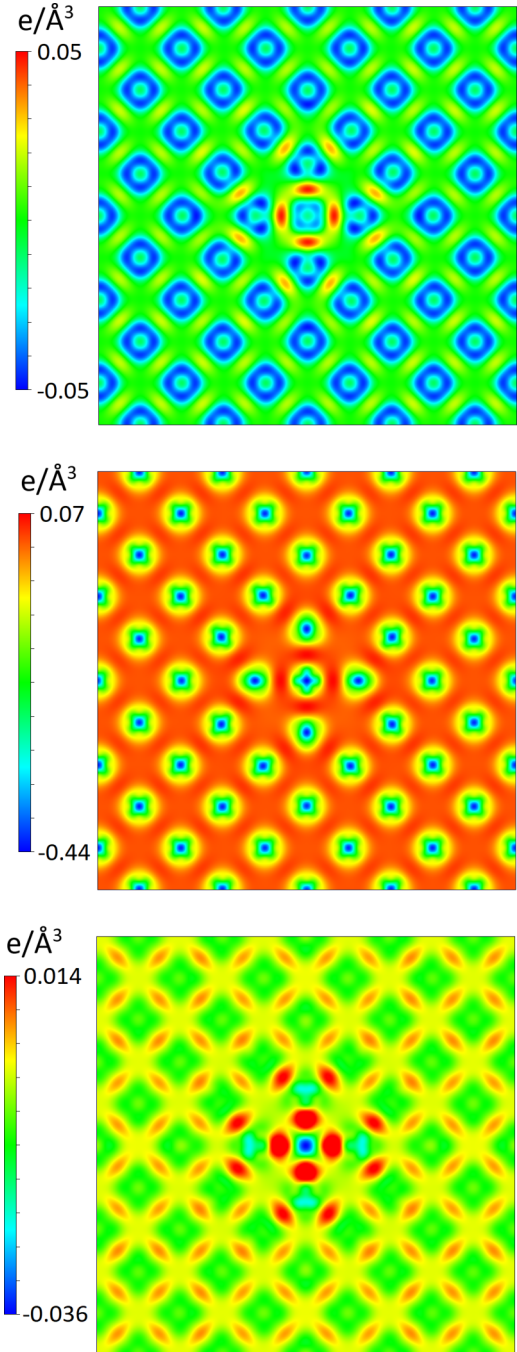


FIG. 15. Two-dimensional plots of electron charge density difference in Al (top), Cu (middle), and Pb (bottom), computed for an octahedral site interstitial configuration in a $\{010\}$ plane.

A schematic illustration of the process is given in Fig. 19. Since the two SIA configurations have almost the same formation energy, the energy required to translate a SIA through the lattice is negligible. This implies that the energy barrier for migration is nearly zero, explaining why T_{ID} in gold is lower than 0.3 K, close to the limit of what can be resolved experimentally. The low temperature character of diffusion of SIA defects in gold is similar to the low temperature one-dimensional diffusion of $\langle 111 \rangle$ crowdions/dumbbells in body-centered cubic metals [15,100,101].

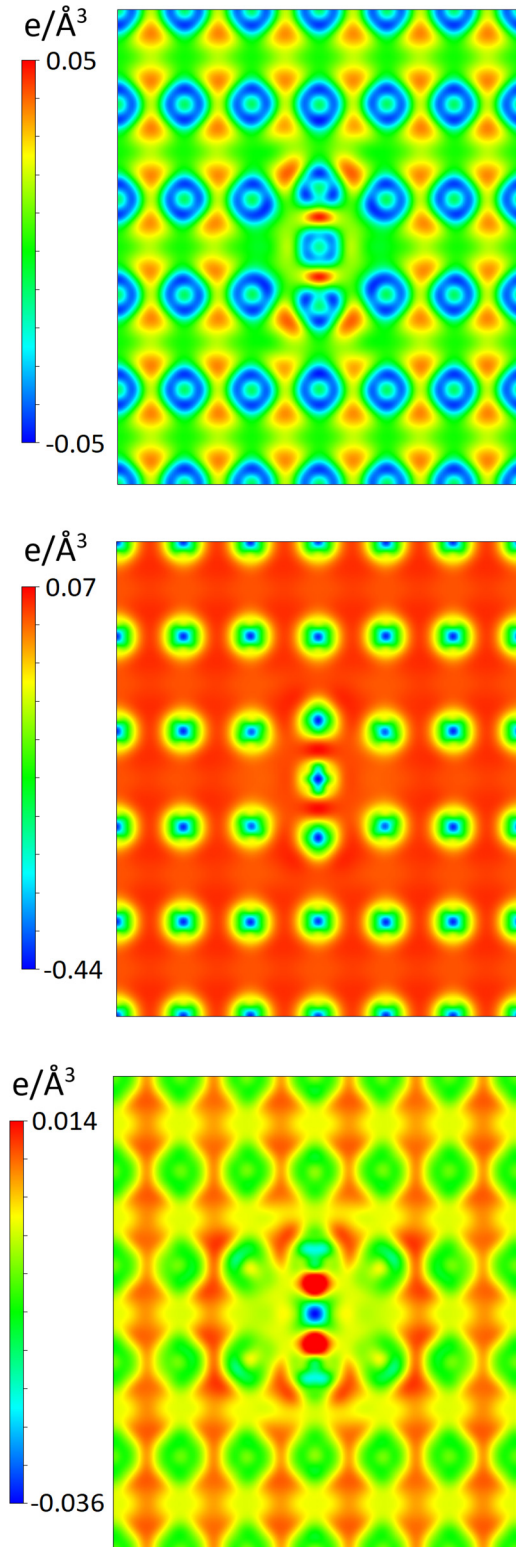


FIG. 16. Two-dimensional plots of electron charge density difference in Al (top), Cu (middle), and Pb (bottom), computed for an octahedral site interstitial configuration in a $\{011\}$ plane.

Elastic dipole tensors P_{ij} of defects fully define their long-range elastic fields [10,14]. The matrix elements and symmetry of the P_{ij} tensor for a particular defect reflects the symmetry of the corresponding SIA configuration. The

TABLE XLII. Experimentally observed values of T_{ID} and migration enthalpy H_i^M taken from Ref. [97].

Element	T_{ID} (K)	H_i^M (eV)
Al	37	0.115/0.112
Ca	—	—
Ni	56	0.15
Cu	38	0.117
Sr	—	—
Rh	32	—
Pd	35	—
Ag	28	0.085/0.088
Ir	50	—
Pt	22	0.065/0.06-0.07 / 0.063
Au	<0.3	—
Pb	4	0.01
Th	10	0.087

dipole character of elastic interaction between defects results in that the energy of interaction depends not only on the relative position of the defects but also on the orientation of the defects with respect to each other [102] and, in an elastically anisotropic material, with respect to the crystal lattice itself [96]. In the limit where the density of defects is low, the P_{ij} -mediated representation of elastic forces can be readily included in simulations like OKMC [32–36] or defect dynamics [37], which show that elastic interactions play an important part in microstructural evolution.

Elastic dipole tensors and relaxation volumes of SIA defects can be determined from diffuse x-ray scattering (DXS) experiments involving samples irradiated with high energy electrons at very low temperature. In Al, the experimentally observed elements of P_{ij} of SIAs are $P_{11} = 15$ eV and $P_{22} = P_{33} = 16$ eV, with the corresponding relaxation volume of the defect $\Omega_{\text{SIA}}^{\text{rel}} = 1.9 \pm 0.4\Omega_0$ [71]. These values compare well with our DFT results. In Cu, Haubold and Martinsen [103] determined that $\text{Tr}(P_{ij}) = \sum_i P_{ii} = 45 \pm 5$ eV, and $(P_{22} - P_{11})/\text{Tr}(P_{ij}) = 0.03 \pm 0.03$ eV, and $\Omega_{\text{SIA}}^{\text{rel}} = 1.45 \pm 0.15\Omega_0$. This corresponds to $P_{11} = 14.1$ eV and $P_{22} = P_{33} = 15.45$ eV

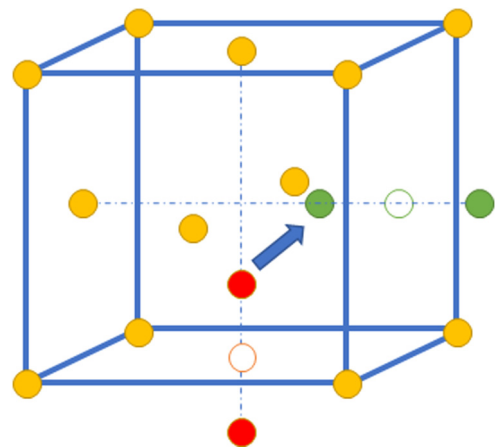


FIG. 17. Schematic illustration of the three-dimensional translation-rotation pathway of migration of a (100) dumbbell from a $[100]$ configuration to a $[010]$ configuration in an FCC crystal.

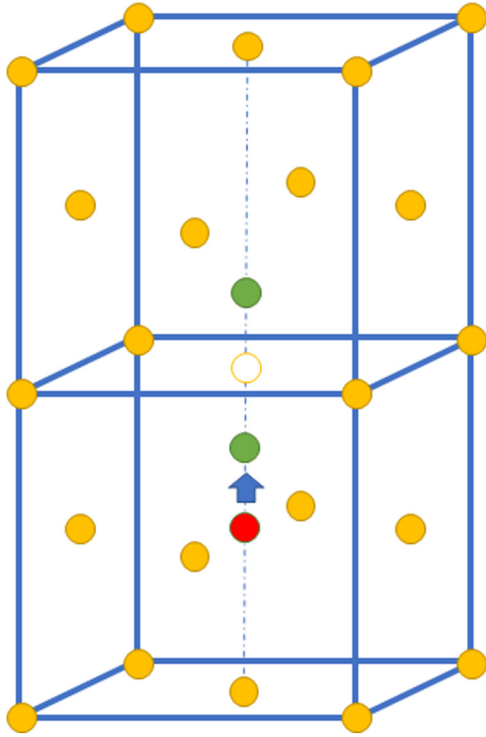


FIG. 18. Schematic illustration of the one-dimensional pathway of migration of an octahedral site interstitial defect in an FCC crystal.

if we convert the matrix elements of the tensor disregarding the experimental uncertainties. A direct comparison shows that our DFT results for Cu are larger than the experimentally observed values. The observed relaxation volume of a defect in Ni is $\Omega_{\text{SIA}}^{\text{rel}}$ is $1.8 \pm 0.2\Omega_0$ [104]. In Pt, the experimentally observed relaxation volume of a SIA defect $\Omega_{\text{SIA}}^{\text{rel}}$ is $2.0 \pm 0.3\Omega_0$ [71]. These values agree well with our first-principles calculations.

Figure 20 shows relaxation volumes of the $\langle 100 \rangle$ dumbbell and octahedral site interstitial defects in metals where calculations were performed using PBE and PBEsol functionals with and without spin-orbit coupling. Similarly to the vacancy case, we find no visible trend that one can attribute to the use of

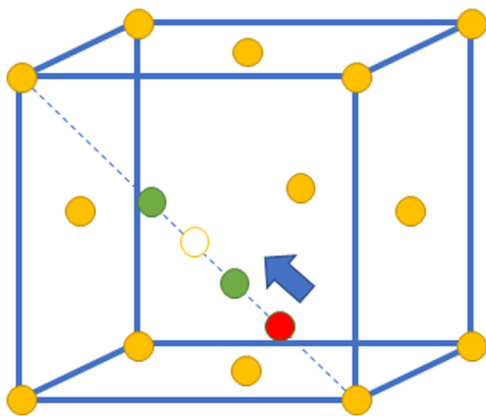


FIG. 19. Schematic illustration of one-dimensional migration of a $\langle 110 \rangle$ crowdion/dumbbell in an FCC crystal.

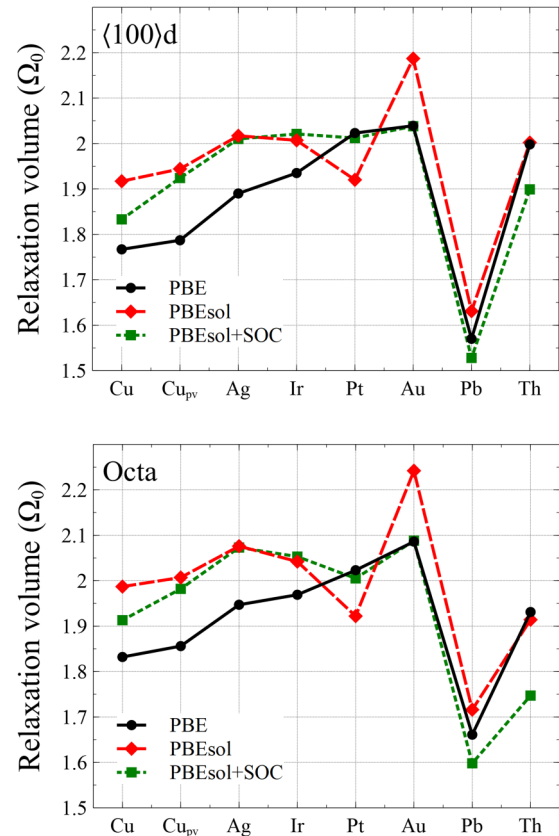


FIG. 20. Relaxation volumes of the $\langle 100 \rangle$ dumbbell and octahedral site interstitial defects, given in atomic volume units Ω_0 , in Cu, Cu_{pv}, Ag, Ir, Pt, Au, Pb, and Th, calculated using exchange-correlation PBE and PBEsol functionals with and without spin-orbit coupling (SOC).

different exchange-correlation functionals or spin-orbit coupling. However, we note that the variation of values computed for a specific element does not exceed 10%.

IV. MAGNETISM OF POINT DEFECT CONFIGURATIONS IN NICKEL

Nickel is a ferromagnetic FCC metal [105]. The most stable SIA defect configuration in nickel is a $\langle 100 \rangle$ dumbbell, and in this respect Ni is similar to many other FCC metals. For comparison, iron (Fe) is also ferromagnetic and an SIA defect in Fe adopts a $\langle 110 \rangle$ dumbbell configuration characterized by the antiferromagnetic ordering of atomic magnetic moments in its core [15,106]. The structure of the SIA defect in Fe is different from the $\langle 111 \rangle$ crowdion/dumbbell configurations typically occurring in BCC metals [15,99]. Magnetism is believed to be responsible for that the structure of an SIA defect in Fe is different from the structure of an SIA defect in other nonmagnetic BCC metals. This warrants a study of magnetism of SIA defect configurations in Ni.

Figure 21 shows a two-dimensional plot of magnetization density, that is the spin up minus the spin down density of electrons, computed for a $\langle 100 \rangle$ dumbbell configuration in Ni in the (010) and (011) planes. Figure 22 is the corresponding two-dimensional plot of the electron charge density

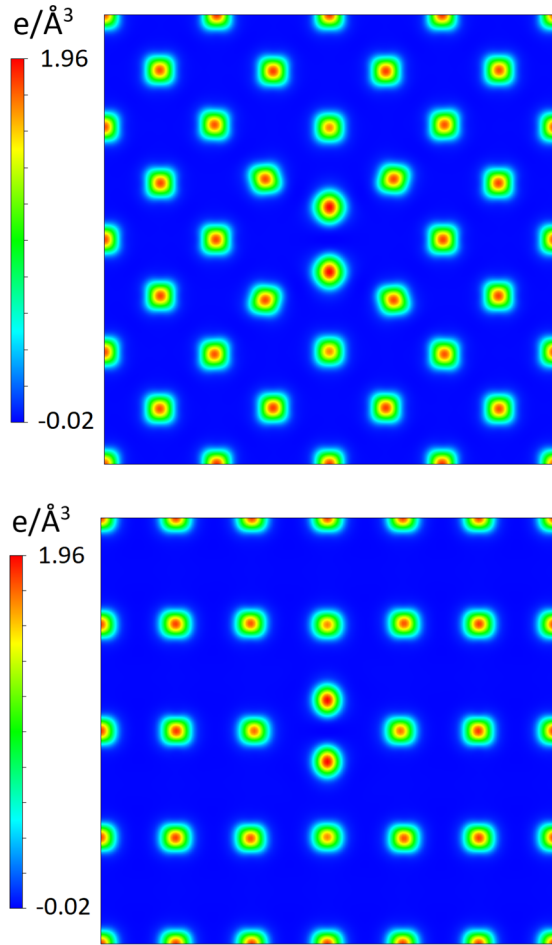


FIG. 21. Two-dimensional plots of magnetization density in nickel, computed for a $\langle 100 \rangle$ dumbbell configuration in (top) $\{010\}$ and (bottom) $\{011\}$ planes.

difference. Interatomic interactions in Ni are mediated by s and d valence electrons, and this agrees with the anisotropic pattern of directional bonds near the core of an SIA defect. Magnetization appears to have an almost negligible effect despite the fact that the core part of the defect is highly compressed. The locally projected magnetic moments of the two atoms in the core of the defect equal $0.721\mu_B$. The magnetic moment of a Ni atom in a perfect FCC lattice at equilibrium is $0.697\mu_B$, according to a calculation performed using a 256 atom cell.

Figure 23 shows the total magnetization and energy of a Ni atom as a function of the lattice constant, calculated using a one-atom FCC unit cell and $21 \times 21 \times 21$ k -points mesh, and the PBE exchange-correlation functional. The curve exhibits a positive monotonic correlation between the magnitude of the magnetic moment of an atom and the available atomic volume. This suggests that if the volume available to an atom is small, its magnetic moment is expected to be small. However, such a rule does not appear to apply to the magnetic moment of atoms in the core of an SIA configuration in Ni. The magnetic moments in the core of the defect are actually larger than the magnetic moments of atoms in the crystal bulk. Besides, the magnetic moments of atoms in the core of the

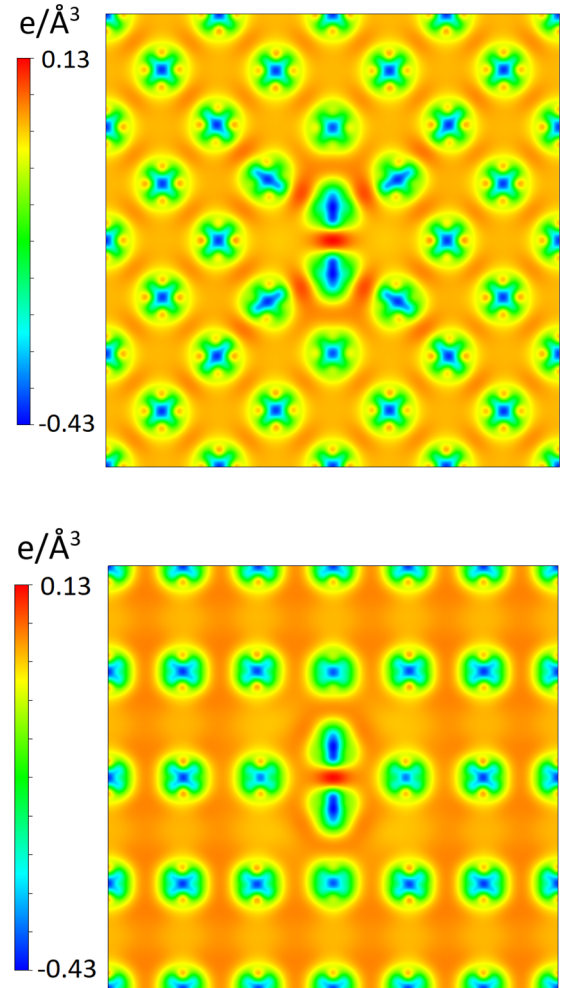


FIG. 22. Two-dimensional plots of electron charge density difference in nickel computed for a $\langle 100 \rangle$ dumbbell configuration in (top) $\{010\}$ and (bottom) $\{011\}$ planes.

defect remain ferromagnetically aligned with the moments of surrounding atoms. This is completely different from the case of Fe, where moments of atoms in the core of a defect are aligned antiferromagnetically with respect to the atoms in the vicinity of the defect [15,99]. These results suggest that magnetism does not have a significant effect on the structure and stability of SIA defects in Ni.

V. MIGRATION OF A SELF-INTERSTITIAL ATOM DEFECT IN COPPER

Copper is one of the most commonly used materials for applications requiring high electric and thermal conductivity. In fusion technology, copper alloys are used as heat sink materials, often in combination with tungsten directly facing the plasma [3]. A self-interstitial atom defect in copper adopts a $\langle 100 \rangle$ dumbbell configuration, which is expected to migrate following a translation-rotation pathway illustrated in Fig. 17 [71–73,98]. Since from each location in the crystal lattice a defect can follow any of the eight available degenerate migration pathways, the defect diffuses three-dimensionally through the lattice.

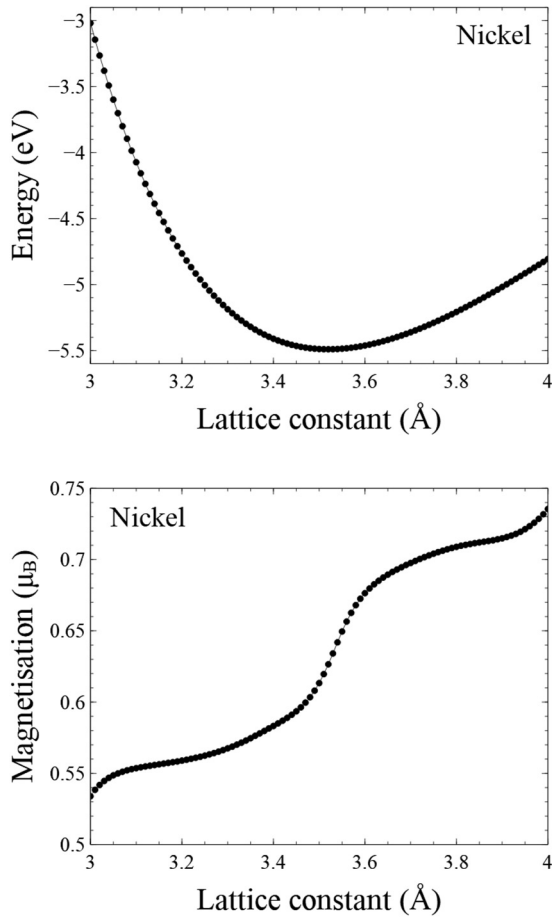


FIG. 23. Energy and magnetic moment of a nickel atom plotted as a function of the FCC lattice constant in a perfect crystal structure.

To explore the dynamics of migration of a defect in copper, we performed a nudged elastic band calculation [107,108] using nine images, representing a trajectory linking the initial and final equilibrium positions of the defect. Calculations were performed using the PBE exchange correlation functional. Figure 24 shows the variation of the defect formation

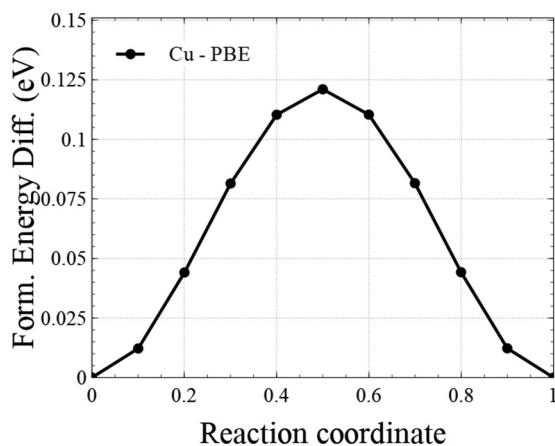


FIG. 24. Variation of the formation energy of a $\langle 100 \rangle$ dumbbell in Cu along the migration pathway of the defect.

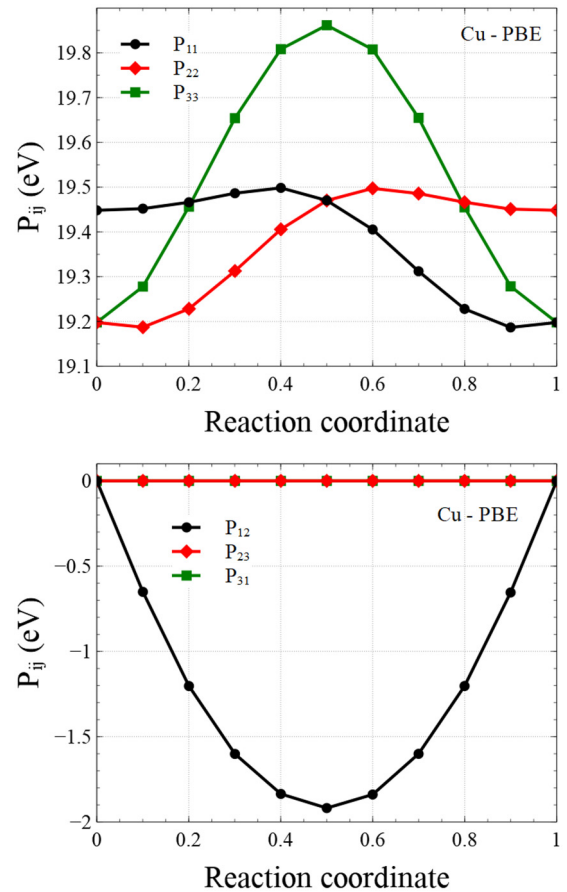


FIG. 25. Variation of elements of elastic dipole tensor of a $\langle 100 \rangle$ dumbbell in Cu along the migration pathway from a $[100]$ to a $[010]$ configuration.

energy as a $\langle 100 \rangle$ dumbbell migrates from the $[100]$ to the $[010]$ configuration along the transition pathway illustrated in Fig. 17. All the defect energies shown in the graph include the elastic correction computed according to Eq. (1). The calculated saddle point energy is 0.121 eV, which compares very well with the experimentally determined migration energy of 0.117 eV [97]. This migration energy is approximately three times lower than the migration energy of an SIA defect in Fe [109].

The variation of elastic dipole tensor and relaxation volume tensor along the migration pathway of the defect are plotted in Figs. 25 and 26, respectively. The graph shows that the elastic field of a $\langle 100 \rangle$ dumbbell follows the transformation of its symmetry as it moves from the initial to the final equilibrium positions as illustrated in Fig. 17. The variation of the relaxation volume along the migration pathway is shown in Fig. 27. The relaxation volume of the defect does not vary significantly along the migration pathway in comparison with its equilibrium initial and final values of $1.767 \Omega_0$.

VI. SUMMARY AND CONCLUSIONS

Using density function theory calculations, we explored the structures of self-interstitial atom (SIA) defects in the most commonly occurring face-centered cubic (FCC) metals. We have computed the formation energies and elastic dipole

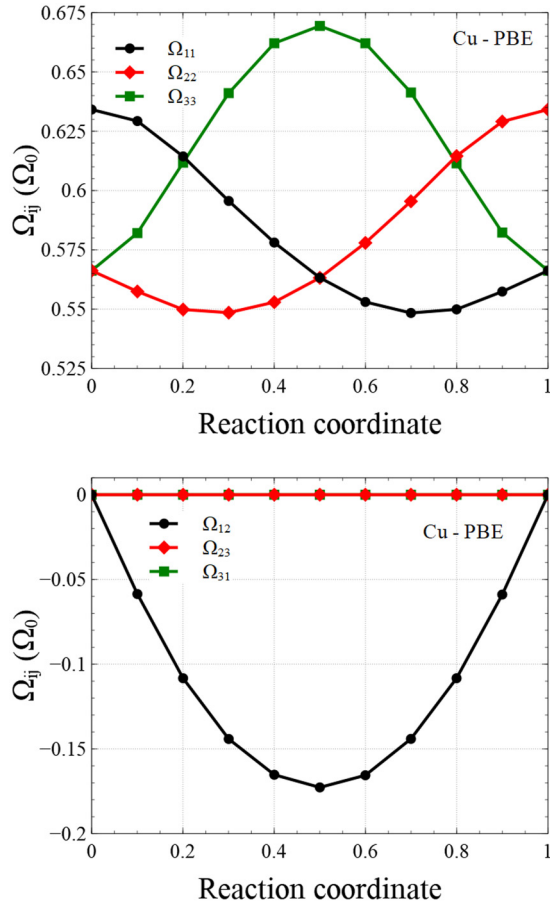


FIG. 26. Variation of elements of the relaxation volume tensor of a $\langle 100 \rangle$ dumbbell in Cu along the migration pathway from a $[100]$ to a $[010]$ configuration.

tensors of all the defect configurations, providing the so far unavailable data required for larger scale simulations of microstructural evolution under extreme conditions. We find that the $\langle 100 \rangle$ SIA defect configuration is not universally stable in all the FCC metals. The most stable SIA configuration in Al, Ca, Ni, Cu, Pd, and Ag is a $\langle 100 \rangle$ dumbbell. The octahedral site SIA configuration is most stable in Pt, Rh, and Th. A $\langle 100 \rangle$ dumbbell configuration of the defect is likely realized in Sr and Ir, whereas a $\langle 110 \rangle$ crowdion/dumbbell

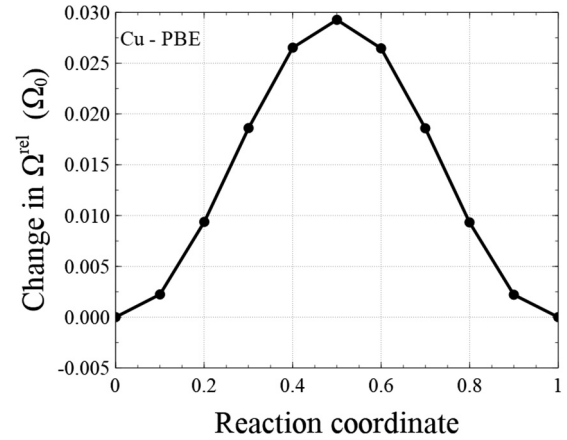


FIG. 27. Variation of the relaxation volume of a $\langle 100 \rangle$ dumbbell in Cu along its migration pathway.

defect represents its lowest energy state in Au. In Pb, a SIA defect adopts an octahedral site configuration. Both the octahedral site SIA defect in Pb and a $\langle 110 \rangle$ crowdion/dumbbell configuration in Au diffuse one-dimensionally through the lattice, as opposed to the three-dimensional translation-rotation diffusion exhibited by the $\langle 100 \rangle$ dumbbells. We find that in nickel, magnetism does not have a notable effect on the structure of point defects. We also explored the variation of elastic parameters of an SIA defect in Cu along its migration pathway, and found that the predicted migration energy compares well with experimental observations.

ACKNOWLEDGMENTS

This work has been carried out within the framework of the EUROfusion Consortium and has received funding from the Euratom research and training programmes 2014-2018 and 2019-2020 under grant Agreement No. 633053 and from the RCUK Energy Programme (Grant No. EP/T012250/1). To obtain further information on the data and models underlying the paper please contact PublicationsManager@ukaea.uk. The views and opinions expressed herein do not necessarily reflect those of the European Commission. We acknowledge computing resources supplied by the IRIS (STFC) Consortium.

- [1] C. K. Gupta, Nuclear reactor materials, in *Encyclopedia of Materials: Science and Technology*, edited by K. H. J. Buschow, R. W. Cahn, M. C. Flemings, B. Ilshner, E. J. Kramer, S. Mahajan, and P. Veyssi re (Elsevier, Oxford, 2001), pp. 6339–6349.
- [2] A. J. H. Donn e and A. W. Morris, *European Research Roadmap to the Realisation of Fusion Energy* (EUROfusion, Garching/Munich, Germany, 2018).
- [3] G. Pintsuk, E. Diegele, S. L. Dudarev, M. Gorley, J. Henry, J. Reiser, and M. Rieth, European materials development: Results and perspective, *Fusion Eng. Des.* **146**, 1300 (2019).
- [4] W. Cai and W. D. Nix, *Imperfections in Crystalline Solids* (Cambridge University Press, Cambridge, England, UK, 2016).
- [5] J. Byggm star, F. Granberg, A. E. Sand, A. Pirttikoski, R. Alexander, M.-C. Marinica, and K. Nordlund, Collision cascades overlapping with self-interstitial defect clusters in Fe and W, *J. Phys.: Condens. Matter* **31**, 245402 (2019).
- [6] A. E. Sand, S. L. Dudarev, and K. Nordlund, High-energy collision cascades in tungsten: Dislocation loops structure and clustering scaling laws, *Europhys. Lett.* **103**, 46003 (2013).
- [7] A. E. Sand, K. Nordlund, and S. L. Dudarev, Radiation damage production in massive cascades initiated by fusion neutrons in tungsten, *J. Nucl. Mater.* **455**, 207 (2014).
- [8] A. E. Sand, M. J. Aliaga, M. J. Caturla, and K. Nordlund, Surface effects and statistical laws of defects in primary radiation damage: Tungsten vs. iron, *Europhys. Lett.* **115**, 36001 (2016).

- [9] A. E. Sand, D. R. Mason, A. De Backer, X. Yi, S. L. Dudarev, and K. Nordlund, Cascade fragmentation: deviation from power law in primary radiation damage, *Mater. Res. Lett.* **5**, 357 (2017).
- [10] S. L. Dudarev, D. R. Mason, E. Tarleton, P.-W. Ma, and A. E. Sand, A multi-scale model for stresses, strains and swelling of reactor components under irradiation, *Nucl. Fusion* **58**, 126002 (2018).
- [11] E. Clouet, S. Garruchet, H. Nguyen, M. Perez, and C. S. Becquart, Dislocation interaction with C in α -Fe: A comparison between atomic simulations and elasticity theory, *Acta Mater.* **56**, 3450 (2008).
- [12] C. Varvenne, F. Bruneval, M.-C. Marinica, and E. Clouet, Point defect modeling in materials: Coupling *ab initio* and elasticity approaches, *Phys. Rev. B* **88**, 134102 (2013).
- [13] C. Varvenne and E. Clouet, Elastic dipoles of point defects from atomistic simulations, *Phys. Rev. B* **96**, 224103 (2017).
- [14] S. L. Dudarev and P.-W. Ma, Elastic fields, dipole tensors, and interaction between self-interstitial atom defects in bcc transition metals, *Phys. Rev. Mater.* **2**, 033602 (2018).
- [15] P.-W. Ma and S. L. Dudarev, Universality of point defect structure in body-centered cubic metals, *Phys. Rev. Mater.* **3**, 013605 (2019).
- [16] P.-W. Ma and S. L. Dudarev, Symmetry-broken self-interstitial defects in chromium, molybdenum, and tungsten, *Phys. Rev. Mater.* **3**, 043606 (2019).
- [17] P.-W. Ma and S. L. Dudarev, Effect of stress on vacancy formation and migration in body-centered-cubic metals, *Phys. Rev. Mater.* **3**, 063601 (2019).
- [18] P.-W. Ma and S. L. Dudarev, CALANIE: Anisotropic elastic correction to the total energy, to mitigate the effect of periodic boundary conditions, *Comput. Phys. Commun.* **252**, 107130 (2020).
- [19] D. R. Mason, S. Das, P. M. Derlet, S. L. Dudarev, A. J. London, H. Yu, N. W. Phillips, D. Yang, K. Mizohata, R. Xu, and F. Hofmann, Observation of Transient and Asymptotic Driven Structural States of Tungsten Exposed to Radiation, *Phys. Rev. Lett.* **125**, 225503 (2020).
- [20] M. Durrand-Charre, *Microstructure of Steels and Cast Irons* (Springer-Verlag, Berlin, 2003).
- [21] F. A. Garner, Radiation-induced damage in austenitic structural steels used in nuclear reactors, in *Comprehensive Nuclear Materials*, edited by R. J. Konings and R. E. Stoller, 2nd ed. (Elsevier, Oxford, 2020), Vol. 3, p. 57.
- [22] P. M. Derlet and S. L. Dudarev, Microscopic structure of a heavily irradiated material, *Phys. Rev. Mater.* **4**, 023605 (2020).
- [23] M. L. Jenkins, M. A. Kirk, and W. J. Phythian, Experimental studies of cascade phenomena in metals, *J. Nucl. Mater.* **205**, 16 (1993).
- [24] B. N. Singh and J. H. Evans, Significant differences in defect accumulation behavior between fcc and bcc crystals under cascade damage conditions, *J. Nucl. Mater.* **226**, 277 (1995).
- [25] B. N. Singh and S. J. Zinkle, Defect accumulation in pure fcc metals in the transient regime: a review, *J. Nucl. Mater.* **206**, 212 (1993).
- [26] A. Chartier and M.-C. Marinica, Rearrangement of interstitial defects in alpha-Fe under extreme condition, *Acta Mater.* **180**, 141 (2019).
- [27] Z. Zhou, M. L. Jenkins, S. L. Dudarev, A. P. Sutton, and M. A. Kirk, Simulations of weak-beam diffraction contrast images of dislocation loops by the many-beam Howie-Basinski equations, *Philos. Mag.* **86**, 4851 (2006).
- [28] X. Yi, A. E. Sand, D. R. Mason, M. A. Kirk, S. G. Roberts, K. Nordlund, and S. L. Dudarev, Direct observation of size scaling and elastic interaction between nano-scale defects in collision cascades, *Europhys. Lett.* **110**, 36001 (2015).
- [29] C. Liu, L. He, Y. Zhai, B. Tyburska-Püschel, P. M. Voyles, K. Sridharan, D. Morgan, and I. Szlufarska, Evolution of small defect clusters in ion-irradiated 3C-SiC: Combined cluster dynamics modeling and experimental study, *Acta Mater.* **125**, 377 (2017).
- [30] B. C. Larson, Historical perspective on diffraction line-profile analyses for crystals containing defect clusters, *Crystals* **9**, 257 (2019).
- [31] S. Dudarev, J.-L. Boutard, R. Lässer, M. Caturla, P. Derlet, M. Fivel, C.-C. Fu, M. Lavrentiev, L. Malerba, M. Mrovec, D. Nguyen-Manh, K. Nordlund, M. Perlado, R. Schäublin, H. V. Swygenhoven, D. Terentyev, J. Wallenius, D. Weygand, and F. Willaime, The EU programme for modeling radiation effects in fusion reactor materials: An overview of recent advances and future goals, *J. Nucl. Mater.* **386–388**, 1 (2009).
- [32] C. Domain, C. S. Becquart, and L. Malerba, Simulation of radiation damage in Fe alloys: An object kinetic Monte Carlo approach, *J. Nucl. Mater.* **335**, 121 (2004).
- [33] I. Martin-Bragado, A. Rivera, G. Valles, J. L. Gomez-Selles, and M. J. Caturla, Mmonca: An object kinetic Monte Carlo simulator for damage irradiation evolution and defect diffusion, *Comput. Phys. Commun.* **184**, 2703 (2013).
- [34] N. Castin, A. Bakaev, G. Bonny, A. Sand, L. Malerba, and D. Terentyev, On the onset of void swelling in pure tungsten under neutron irradiation: An object kinetic Monte Carlo approach, *J. Nucl. Mater.* **493**, 280 (2017).
- [35] A. Vattré, T. Jourdan, H. Ding, M.-C. Marinica, and M. J. Demkowicz, Non-random walk diffusion enhances the sink strength of semicoherent interfaces, *Nat. Commun.* **7**, 10424 (2016).
- [36] D. Carpentier, T. Jourdan, Y. Le Bouar, and M.-C. Marinica, Effect of saddle point anisotropy of point defects on their absorption by dislocations and cavities, *Acta Mater.* **136**, 323 (2017).
- [37] F. Baraglia and P.-W. Ma, Dynamic model for an ensemble of interacting irradiation-induced defects in a macroscopic sample, *Modell. Simul. Mater. Sci. Eng.* (2020), doi: 10.1088/1361-651X/abd014.
- [38] S. L. Dudarev, Density functional theory models for radiation damage, *Annu. Rev. Mater. Res.* **43**, 35 (2013).
- [39] G. H. Kinchin and R. S. Pease, The displacement of atoms in solids by radiation, *Rep. Prog. Phys.* **18**, 1 (1955).
- [40] A. D. Vita and M. J. Gillan, The *ab initio* calculation of defect energetics in aluminium, *J. Phys.: Condens. Matter* **3**, 6225 (1991).
- [41] M. J. Mehl and B. M. Klein, All-electron first-principles supercell total-energy calculation of the vacancy formation energy in aluminium, *Phys. B: Condens. Matter* **172**, 211 (1991).
- [42] B. Drittler, M. Weinert, R. Zeller, and P. H. Dederichs, Vacancy formation energies of fcc transition metals calculated by a full potential green's function method, *Solid State Commun.* **79**, 31 (1991).

- [43] P. H. Dederichs, T. Hoshino, B. Drittler, K. Abraham, and R. Zeller, Total-energy calculations for point defects in metals, *Phys. B: Condens. Matter* **172**, 203 (1991).
- [44] H. M. Polatoglou, M. Methfessel, and M. Scheffler, Vacancy-formation energies at the (111) surface and in bulk Al, Cu, Ag, and Rh, *Phys. Rev. B* **48**, 1877 (1993).
- [45] O. Le Bacq, F. Willaime, and A. Pasturel, Unrelaxed vacancy formation energies in group-IV elements calculated by the full-potential linear muffin-tin orbital method: Invariance with crystal structure, *Phys. Rev. B* **59**, 8508 (1999).
- [46] P. A. Korzhavyi, I. A. Abrikosov, B. Johansson, A. V. Ruban, and H. L. Skriver, First-principles calculations of the vacancy formation energy in transition and noble metals, *Phys. Rev. B* **59**, 11693 (1999).
- [47] K. Carling, G. Wahnström, T. R. Mattsson, A. E. Mattsson, N. Sandberg, and G. Grimvall, Vacancies in Metals: From First-Principles Calculations to Experimental Data, *Phys. Rev. Lett.* **85**, 3862 (2000).
- [48] T. Mizuno, M. Asato, T. Hoshino, and K. Kawakami, First-principles calculations for vacancy formation energies in Ni and Fe: non-local effect beyond the LSDA and magnetism, *J. Magn. Magn. Mater.* **226-230**, 386 (2001).
- [49] T. Hoshino, T. Mizuno, M. Asato, and H. Fukushima, Full-potential KKR calculations for point defect energies in metals, based on the generalized-gradient approximation: I. vacancy formation energies in fcc and bcc metals, *Mater. Trans.* **42**, 2206 (2001).
- [50] R. P. Kauffman and A. M. Rappe, Vacancies below the (111) surface of Pd, *Phys. Rev. B* **67**, 085403 (2003).
- [51] D. A. Andersson and S. I. Simak, Monovacancy and divacancy formation and migration in copper: A first-principles theory, *Phys. Rev. B* **70**, 115108 (2004).
- [52] E. H. Megchiche, S. Pérusin, J.-C. Barthelat, and C. Mijoule, Density functional calculations of the formation and migration enthalpies of monovacancies in Ni: Comparison of local and nonlocal approaches, *Phys. Rev. B* **74**, 064111 (2006).
- [53] G. Ho, M. T. Ong, K. J. Caspersen, and E. A. Carter, Energetics and kinetics of vacancy diffusion and aggregation in shocked aluminium via orbital-free density functional theory, *Phys. Chem. Chem. Phys.* **9**, 4951 (2007).
- [54] M. Mantina, Y. Wang, R. Arroyave, L. Q. Chen, Z. K. Liu, and C. Wolverton, First-Principles Calculation of Self-Diffusion Coefficients, *Phys. Rev. Lett.* **100**, 215901 (2008).
- [55] O. Y. Vekilova, D. I. Bazhanov, S. I. Simak, and I. A. Abrikosov, First-principles study of vacancy-hydrogen interaction in Pd, *Phys. Rev. B* **80**, 024101 (2009).
- [56] L. Delczeg, E. K. Delczeg-Czirjak, B. Johansson, and L. Vitos, Assessing common density functional approximations for the *ab initio* description of monovacancies in metals, *Phys. Rev. B* **80**, 205121 (2009).
- [57] R. Nazarov, T. Hickel, and J. Neugebauer, Vacancy formation energies in fcc metals: Influence of exchange-correlation functionals and correction schemes, *Phys. Rev. B* **85**, 144118 (2012).
- [58] A. Metsue, A. Oudriss, J. Bouhattate, and X. Feugas, Contribution of the entropy on the thermodynamic equilibrium of vacancies in nickel, *J. Chem. Phys.* **140**, 104705 (2014).
- [59] T. Angsten, T. Mayeshiba, H. Wu, and D. Morgan, Elemental vacancy diffusion database from high-throughput first-principles calculations for fcc and hcp structures, *New J. Phys.* **16**, 015018 (2014).
- [60] C. Z. Hargather, S.-L. Shang, Z.-K. Liu, and Y. Du, A first-principles study of self-diffusion coefficients of fcc Ni, *Comput. Mater. Sci.* **86**, 17 (2014).
- [61] M. Iyer, V. Gavini, and T. M. Pollock, Energetics and nucleation of point defects in aluminum under extreme tensile hydrostatic stresses, *Phys. Rev. B* **89**, 014108 (2014).
- [62] D. Connétable, E. Andrieu, and D. Monceau, First-principles nickel database: Energetics of impurities and defects, *Comput. Mater. Sci.* **101**, 77 (2015).
- [63] S.-L. Shang, B.-C. Zhou, W. Y. Wang, A. J. Ross, X. L. Liu, Y.-J. Hu, H.-Z. Fang, Y. Wang, and Z.-K. Liu, A comprehensive first-principles study of pure elements: Vacancy formation and migration energies and self-diffusion coefficients, *Acta Mater.* **109**, 128 (2016).
- [64] Y. Gong, B. Grabowski, A. Glensk, F. Körmann, J. Neugebauer, and R. C. Reed, Temperature dependence of the Gibbs energy of vacancy formation of fcc Ni, *Phys. Rev. B* **97**, 214106 (2018).
- [65] A. Glensk, B. Grabowski, T. Hickel, and J. Neugebauer, Breakdown of the Arrhenius Law in Describing Vacancy Formation Energies: The Importance of Local Anharmonicity Revealed by *Ab Initio* Thermodynamics, *Phys. Rev. X* **4**, 011018 (2014).
- [66] R. Qiu, H. Lu, B. Ao, L. Huang, T. Tang, and P. Chen, Energetics of intrinsic point defects in aluminium via orbital-free density functional theory, *Philos. Mag.* **97**, 2164 (2017).
- [67] B. J. Jesson, M. Foley, and P. A. Madden, Thermal properties of the self-interstitial in aluminum: An *ab initio* molecular-dynamics study, *Phys. Rev. B* **55**, 4941 (1997).
- [68] J. D. Tucker, T. R. Allen, and D. Morgan, *Ab Initio* defect properties for modeling radiation-induced segregation in Fe-Ni-Cr alloys, in *13th International Conference on Environmental Degradation of Materials in Nuclear Power Systems, Whistler, BC, Canada, April 19* (Canadian Nuclear Society, Ontario, Canada, 2007), Vol. 23, pp. 1004–14.
- [69] R. Q. Hood, P. R. C. Kent, and F. A. Reboredo, Diffusion quantum Monte Carlo study of the equation of state and point defects in aluminum, *Phys. Rev. B* **85**, 134109 (2012).
- [70] W. M. C. Foulkes, L. Mitas, R. J. Needs, and G. Rajagopal, Quantum Monte Carlo simulations of solids, *Rev. Mod. Phys.* **73**, 33 (2001).
- [71] W. Schilling, Self-interstitial atoms in metals, *J. Nucl. Mater.* **69-70**, 465 (1978).
- [72] P. Ehrhart, The configuration of atomic defects as determined from scattering studies, *J. Nucl. Mater.* **69-70**, 200 (1978).
- [73] P. H. Dederichs, C. Lehmann, H. R. Schober, A. Scholz, and R. Zeller, Lattice theory of point defects, *J. Nucl. Mater.* **69-70**, 176 (1978).
- [74] G. Kresse and J. Hafner, *Ab initio* molecular dynamics for liquid metals, *Phys. Rev. B* **47**, 558 (1993).
- [75] G. Kresse and J. Hafner, *Ab initio* molecular-dynamics simulation of the liquid-metal–amorphous-semiconductor transition in germanium, *Phys. Rev. B* **49**, 14251 (1994).
- [76] G. Kresse and J. Furthmüller, Efficiency of *ab initio* total energy calculations for metals and semiconductors using a plane-wave basis set, *Comput. Mater. Sci.* **6**, 15 (1996).

- [77] G. Kresse and J. Furthmüller, Efficient iterative schemes for *ab initio* total-energy calculations using a plane-wave basis set, *Phys. Rev. B* **54**, 11169 (1996).
- [78] P. E. Blöchl, Projector augmented-wave method, *Phys. Rev. B* **50**, 17953 (1994).
- [79] G. Kresse and D. Joubert, From ultrasoft pseudopotentials to the projector augmented-wave method, *Phys. Rev. B* **59**, 1758 (1999).
- [80] J. P. Perdew, K. Burke, and M. Ernzerhof, Generalized Gradient Approximation Made Simple, *Phys. Rev. Lett.* **77**, 3865 (1996).
- [81] J. P. Perdew, K. Burke, and M. Ernzerhof, Erratum: Generalized Gradient Approximation Made Simple [Phys. Rev. Lett. **77**, 3865 (1996)], *Phys. Rev. Lett.* **78**, 1396(E) (1997).
- [82] J. P. Perdew, A. Ruzsinszky, G. I. Csonka, O. A. Vydrov, G. E. Scuseria, L. A. Constantin, X. Zhou, and K. Burke, Restoring the Density-Gradient Expansion for Exchange in Solids and Surfaces, *Phys. Rev. Lett.* **100**, 136406 (2008).
- [83] J. P. Perdew, A. Ruzsinszky, G. I. Csonka, O. A. Vydrov, G. E. Scuseria, L. A. Constantin, X. Zhou, and K. Burke, Erratum: Restoring the Density-Gradient Expansion for Exchange in Solids and Surfaces [Phys. Rev. Lett. **100**, 136406 (2008)], *Phys. Rev. Lett.* **102**, 039902(E) (2009).
- [84] J. P. Perdew, A. Ruzsinszky, G. I. Csonka, L. A. Constantin, and J. Sun, Workhorse Semilocal Density Functional for Condensed Matter Physics and Quantum Chemistry, *Phys. Rev. Lett.* **103**, 026403 (2009).
- [85] J. Sun, M. Marsman, G. I. Csonka, A. Ruzsinszky, P. Hao, Y.-S. Kim, G. Kresse, and J. P. Perdew, Self-consistent meta-generalized gradient approximation within the projector-augmented-wave method, *Phys. Rev. B* **84**, 035117 (2011).
- [86] A. D. Corso and A. Mosca Conte, Spin-orbit coupling with ultrasoft pseudopotentials: Application to Au and Pt, *Phys. Rev. B* **71**, 115106 (2005).
- [87] N. E. Christensen and B. O. Seraphin, Relativistic band calculation and the optical properties of gold, *Phys. Rev. B* **4**, 3321 (1971).
- [88] T. Rangel, D. Kecik, P. E. Trevisanutto, G.-M. Rignanese, H. Van Swygenhoven, and V. Olevano, Band structure of gold from many-body perturbation theory, *Phys. Rev. B* **86**, 125125 (2012).
- [89] A. E. Shields, D. Santos-Carballal, and N. H. de Leeuw, A density functional theory study of uranium-doped thoria and uranium adatoms on the major surfaces of thorium dioxide, *J. Nucl. Mater.* **473**, 99 (2016).
- [90] S. L. Dudarev, P. Liu, D. A. Andersson, C. R. Stanek, T. Ozaki, and C. Franchini, Parametrization of LSDA+U for noncollinear magnetic configurations: Multipolar magnetism in UO₂, *Phys. Rev. Mater.* **3**, 083802 (2019).
- [91] J. Tao, J. P. Perdew, V. N. Staroverov, and G. E. Scuseria, Climbing the Density Functional Ladder: Nonempirical Meta-Generalized Gradient Approximation Designed for Molecules and Solids, *Phys. Rev. Lett.* **91**, 146401 (2003).
- [92] M. Ropo, K. Kokko, and L. Vitos, Assessing the Perdew-Burke-Ernzerhof exchange-correlation density functional revised for metallic bulk and surface systems, *Phys. Rev. B* **77**, 195445 (2008).
- [93] B. Medasani, M. Haranczyk, A. Canning, and M. Asta, Vacancy formation energies in metals: A comparison of MetaGGA with LDA and GGA exchange-correlation functionals, *Comput. Mater. Sci.* **101**, 96 (2015).
- [94] Y. Le Page and P. Saxe, Symmetry-general least-squares extraction of elastic data for strained materials from *ab initio* calculations of stress, *Phys. Rev. B* **65**, 104104 (2002).
- [95] S. Kurth, J. P. Perdew, and P. Blaha, Molecular and solid-state tests of density functional approximations: LSD, GGAs, and meta-GGAs, *Int. J. Quantum Chem.* **75**, 889 (1999).
- [96] G. Leibfried and N. Breuer, *Point Defects in Metals* (Springer, Berlin, 1978), p. 161.
- [97] P. Ehrhart, P. Jung, H. Schultz, and H. Ullmaier, in *Atomic Defects in Metals*, edited by H. Ullmaier, Landolt-Börnstein - Group III Condensed Matter Vol. 25 (Springer-Verlag, Berlin Heidelberg, 1991).
- [98] V. Spirić, L. E. Rehn, K.-H. Robrock, and W. Schilling, Anelastic relaxation due to single self-interstitial atoms in electron-irradiated Al, *Phys. Rev. B* **15**, 672 (1977).
- [99] D. Nguyen-Manh, A. P. Horsfield, and S. L. Dudarev, Self-interstitial atom defects in bcc transition metals: Group-specific trends, *Phys. Rev. B* **73**, 020101(R) (2006).
- [100] T. D. Swinburne, P.-W. Ma, and S. L. Dudarev, Low temperature diffusivity of self-interstitial defects in tungsten, *New J. Phys.* **19**, 073024 (2017).
- [101] K. Arakawa, M.-C. Marinica, S. Fitzgerald, L. Proville, D. Nguyen-Manh, S. L. Dudarev, P.-W. Ma, T. D. Swinburne, A. M. Goryaeva, T. Yamada, T. Amino, S. Arai, Y. Yamamoto, K. Higuchi, N. Tanaka, H. Yasuda, T. Yasuda, and H. Mori, Quantum de-trapping and transport of heavy defects in tungsten, *Nat. Mater.* **19**, 508 (2020).
- [102] S. Dudarev and A. Sutton, Elastic interactions between nanoscale defects in irradiated materials, *Acta Mater.* **125**, 425 (2017).
- [103] H.-G. Haubold and D. Martinsen, Structure determination of self-interstitials and investigation of vacancy clustering in copper by diffuse X-ray scattering, *J. Nucl. Mater.* **69-70**, 644 (1978).
- [104] O. Bender and P. Ehrhart, Self-interstitial atoms, vacancies and their agglomerates in electron-irradiated nickel investigated by diffuse scattering of X-rays, *J. Phys. F* **13**, 911 (1983).
- [105] J. C. Slater, The ferromagnetism of nickel, *Phys. Rev.* **49**, 537 (1936).
- [106] C. Domain and C. S. Becquart, *Ab initio* calculations of defects in Fe and dilute Fe-Cu alloys, *Phys. Rev. B* **65**, 024103 (2001).
- [107] G. Mills, H. Jónsson, and G. K. Schenter, Reversible work transition state theory: Application to dissociative adsorption of hydrogen, *Surf. Sci.* **324**, 305 (1995).
- [108] H. Jónsson, G. Mills, and K. W. Jacobsen, Nudged elastic band method for finding minimum energy paths of transitions, *Classical and Quantum Dynamics in Condensed Phase Simulations* (World Scientific, Singapore, 1998), pp. 385–404.
- [109] C.-C. Fu, F. Willaime, and P. Ordejón, Stability and Mobility of Mono- and Di-Interstitials in α -Fe, *Phys. Rev. Lett.* **92**, 175503 (2004).
- [110] A. G. Every and A. K. McCurdy, in *Second and Higher Order Elastic Constants*, edited by D. F. Nelson, Landolt-Börnstein - Group III Condensed Matter Vol. 29A (Springer-Verlag, Berlin Heidelberg, 1992), pp. 11–17, Table 3.
- [111] C. Kittel, *Introduction to Solid State Physics*, 8th ed. (Wiley, New York, 2004).